
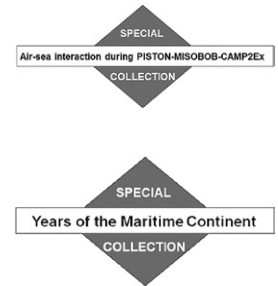


## The Coupling Between Tropical Meteorology, Aerosol Lifecycle, Convection, and Radiation during the Cloud, Aerosol and Monsoon Processes Philippines Experiment (CAMP<sup>2</sup>Ex)

J. S. Reid , H. B. Maring, G. T. Narisma, S. van den Heever, L. Di Girolamo, R. Ferrare, P. Lawson, G. G. Mace, J. B. Simpas, S. Tanelli, L. Ziemba, B. van Dienenhoven, R. Brientjes, A. Bucholtz, B. Cairns, M. O. Cambaliza, G. Chen, G. S. Diskin, J. H. Flynn, C. A. Hostetler, R. E. Holz, T. J. Lang, K. S. Schmidt, G. Smith, A. Sorooshian, E. J. Thompson, K. L. Thornhill, C. Trepte, J. Wang, S. Woods, S. Yoon, M. Alexandrov, S. Alvarez, C. G. Amiot, J. R. Bennett, M. Brooks, S. P. Burton, E. Cayan, H. Chen, A. Collow, E. Crosbie, A. DaSilva, J. P. DiGangi, D. D. Flagg, S. W. Freeman, D. Fu, E. Fukada, M. R. A. Hilario, Y. Hong, S. M. Hristova-Veleva, R. Kuehn, R. S. Kowch, G. R. Leung, J. Lloveridge, K. Meyer, R. M. Miller, M. J. Montes, J. N. Moum, A. Nenes, S. W. Nesbitt, M. Norgren, E. P. Nowottnick, R. M. Rauber, E. A. Reid, S. Rutledge, J. S. Schlosser, T. T. Sekiyama, M. A. Shook, G. A. Sokolowsky, S. A. Stamnes, T. Y. Tanaka, A. Wasilewski, P. Xian, Q. Xiao, Zhuocan Xu, and J. Zavaleta



**ABSTRACT:** The NASA Cloud, Aerosol, and Monsoon Processes Philippines Experiment (CAMP<sup>2</sup>Ex) employed the NASA P-3, Stratton Park Engineering Company (SPEC) Learjet 35, and a host of satellites and surface sensors to characterize the coupling of aerosol processes, cloud physics, and atmospheric radiation within the Maritime Continent’s complex southwest monsoonal environment. Conducted in the late summer of 2019 from Luzon, Philippines, in conjunction with the Office of Naval Research Propagation of Intraseasonal Tropical Oscillations (PISTON) experiment with its R/V *Sally Ride* stationed in the northwestern tropical Pacific, CAMP<sup>2</sup>Ex documented diverse biomass burning, industrial and natural aerosol populations, and their interactions with small to congestus convection. The 2019 season exhibited El Niño conditions and associated drought, high biomass burning emissions, and an early monsoon transition allowing for observation of pristine to massively polluted environments as they advected through intricate diurnal mesoscale and radiative environments into the monsoonal trough. CAMP<sup>2</sup>Ex’s preliminary results indicate 1) increasing aerosol loadings tend to invigorate congestus convection in height and increase liquid water paths; 2) lidar, polarimetry, and geostationary Advanced Himawari Imager remote sensing sensors have skill in quantifying diverse aerosol and cloud properties and their interaction; and 3) high-resolution remote sensing technologies are able to greatly improve our ability to evaluate the radiation budget in complex cloud systems. Through the development of innovative informatics technologies, CAMP<sup>2</sup>Ex provides a benchmark dataset of an environment of extremes for the study of aerosol, cloud, and radiation processes as well as a crucible for the design of future observing systems.

<https://doi.org/10.1175/BAMS-D-21-0285.1>

Corresponding author: Jeffrey S. Reid, [jeffrey.reid@nrlmry.navy.mil](mailto:jeffrey.reid@nrlmry.navy.mil)

Supplemental material: <https://doi.org/10.1175/BAMS-D-21-0285.2>

In final form 21 December 2022

© 2023 American Meteorological Society. This published article is licensed under the terms of a Creative Commons Attribution 4.0 International (CC BY 4.0) License



**KEYWORDS:** Atmosphere; Maritime Continent; Monsoons; Aerosols; Cloud microphysics; Radiative fluxes

**AFFILIATIONS:** Reid, Bucholtz,\* Flagg, Reid, and Xian—U.S. Naval Research Laboratory, Monterey, California; Maring—NASA Headquarters, Washington, D.C.; Narisma,\* Simpas, and Cambaliza—Manila Observatory and Ateneo de Manila University, Metro Manila, Philippines; van den Heever, Freeman, Rutledge, and Sokolowsky—Colorado State University, Ft. Collins, Colorado; Di Girolamo, Fu, Hong, Loveridge, Miller, Nesbitt, and Rauber—University of Illinois Urbana–Champaign, Urbana, Illinois; Ferrare, Ziemba, Chen, Diskin, Hostetler, Trepte, Burton, DiGangi, Shook, and Stamnes—NASA Langley Research Center, Hampton, Virginia; Lawson and Woods—Stratton Park Engineering Co., Boulder, Colorado; Mace and Xu—University of Utah, Salt Lake City, Utah; Tanelli and Hristova-Veleva—Jet Propulsion Laboratory, California Institute of Technology, Pasadena, California; van Diedenhoven\*—NASA Goddard Institute for Space Sciences, and Columbia University, New York, New York; Bruintjes—National Center for Atmospheric Research, Boulder, Colorado; Cairns—NASA Goddard Institute for Space Sciences, New York, New York; Flynn, Yoon, and Alvarez—University of Houston, Houston, Texas; Holz and Kuehn—University of Wisconsin–Madison, Madison, Wisconsin; Lang—NASA Marshall Space Flight Center, Huntsville, Alabama; Schmidt, Chen, and Norgren—University of Colorado Boulder, Boulder, Colorado; Smith and Montes—U.S. Naval Research Laboratory, Washington, D.C.; Sorooshian and Schlosser—The University of Arizona, Tucson, Arizona; Thompson—NOAA/Physical Sciences Laboratory, Boulder, Colorado; Thornhill, Kowch, and Crosbie—Science Systems and Applications, Inc. at NASA Langley Research Center, Hampton, Virginia; Wang and Xiao—Washington University, St. Louis, Missouri; Alexandrov—Columbia University, New York, New York; Amiot—University of Alabama in Huntsville, Huntsville, Alabama; Bennett—Bay Area Environmental Research Institute, NASA Ames Research Center, Moffett Field, California; Brooks—Met Office, Exeter, United Kingdom; Cayan—Philippine Atmospheric, Geophysical and Astronomical Services Administration, Metro Manila, Philippines; Collow—University of Maryland, Baltimore County, and NASA Goddard Space Flight Center, Greenbelt, Maryland; DaSilva, Meyer, and Nowotnick—NASA Goddard Space Flight Center, Greenbelt, Maryland; Fukada—General Dynamics Information Technology, U.S. Naval Research Laboratory, Monterey, California; Hilario—The University of Arizona, Tucson, Arizona, and Manila Observatory and Ateneo de Manila University, Metro Manila, Philippines; Leung—Colorado State University, Ft. Collins, Colorado, and Manila Observatory and Ateneo de Manila University, Metro Manila, Philippines; Moum—Oregon State University, Corvallis, Oregon; Nenes\*—Georgia Institute of Technology, Atlanta, Georgia; Sekiyama and Tanaka—Japan Meteorological Agency, Tsukuba, Japan; Wasilewski—SciSPACE LLC, and NASA Goddard Institute for Space Sciences, New York, New York; Zavaleta—NASA Ames Research Center, Moffett Field, California

\* **CURRENT AFFILIATIONS:** Bucholtz—Naval Postgraduate School, Monterey, California; van Diedenhoven—SRON Netherlands Institute for Space Research, Leiden, Netherlands; Nenes—Ecole Polytechnique Fédérale de Lausanne, Lausanne, Switzerland

+ Deceased.

The Maritime Continent (MC) of Southeast Asia, comprising the archipelago of islands from the Malay Peninsula through Indonesian New Guinea and the Philippines, hosts some of the world's most complex aerosol, cloud, and coupled ocean–terrestrial–atmospheric systems. With its steep topography situated in the Pacific warm pool, the MC is an important contributor to Earth's moisture, energy, and vertical transport budgets far outside its tropical latitude range (e.g., Ramage 1968; Jin and Hoskins 1995; Neale and Slingo 2003; Carminati et al. 2014). High levels of pollution and biomass burning emissions contrast with natural marine and biogenic aerosol sources. Burning for agriculture and urbanization occurs at significant rates (Miettinen et al. 2016). These burning emissions are strongly tied to precipitation anomalies associated with numerous interseasonal and intraseasonal cycles (Field and Shen 2008; Reid et al. 2012, 2013; Field et al. 2016) and a nonlinear hydrological response (Taufik et al. 2017). The region further includes significant anthropogenic emissions from heavy industry, mobile sources, and biofuel (e.g., Balasubramanian et al. 2003; Lee et al. 2019; Chen et al. 2020). The resulting regional-scale air quality events are among the worst in the world with adverse health outcomes and economic feedback (e.g., Kim et al. 2015; Crippa et al. 2016; Koplitz et al. 2016, 2017; Lee et al. 2018, 2019). Increasing emissions coincide with climatic change in temperature and rainfall within a region already vulnerable to weather extremes (e.g., Endo et al. 2009; Yusef and Francisco 2009; IPCC 2013, 2014; Deni et al. 2010; Cruz et al. 2013; Cinco et al. 2014; Villafuerte et al. 2014; Olaguera et al. 2018; Bagtasa 2020).

Clouds within the MC exist in a spectrum of pristine through highly polluted regimes and likely demonstrate aerosol particle, microphysics, precipitation, and radiation interdependencies. Observational evidence suggests higher aerosol loadings result in 1) enhanced warm cloud albedo in Southeast Asia (Sorooshian et al. 2009, 2013; Ross et al. 2018) due to reduced droplet size, through the Twomey effect (Twomey 1974, 1977); 2) indicators of aerosol-related storm invigoration have been observed through enhanced lightning (e.g., Yuan et al. 2011; Thornton et al. 2017); and 3) suppressed warm rain and enhanced deep-convection-related precipitation processes (e.g., Rosenfeld and Lensky 1998; Rosenfeld 1999). While it is unclear how aerosol impacts differ in terrestrial versus maritime environments, we expect findings from other regions and modeling studies to have some applicability to the MC. These include a host of aerosol-induced micro- and macrophysical changes in clouds (e.g., Tao et al. 2012; Dey et al. 2011), such as delays in warm rain formation (Berg et al. 2008) and congestus and overall storm invigoration (e.g., Lyons et al. 1998; Wang et al. 2009; Storer et al. 2014). Modeling studies are largely consistent in warm-phase cloud processes, but less so as ice nucleation begins to take hold (Khain et al. 2005; van den Heever et al. 2006; Saleeby et al. 2010; Cotton et al. 2012; Fan et al. 2013; Grant and van den Heever 2015; Sheffield et al. 2015; Mace and Abernathy 2016; Gryspeerdt et al. 2017). At the same time, radiation perturbations by particles feed back into atmospheric stability and cloud formation (Ackerman et al. 2000; Sokolowsky et al. 2022). In sum, aerosol particle impacts on cloud processes are coupled to aerosol life cycle, the radiative budget, and feedback to cloud microphysical and dynamical processes.

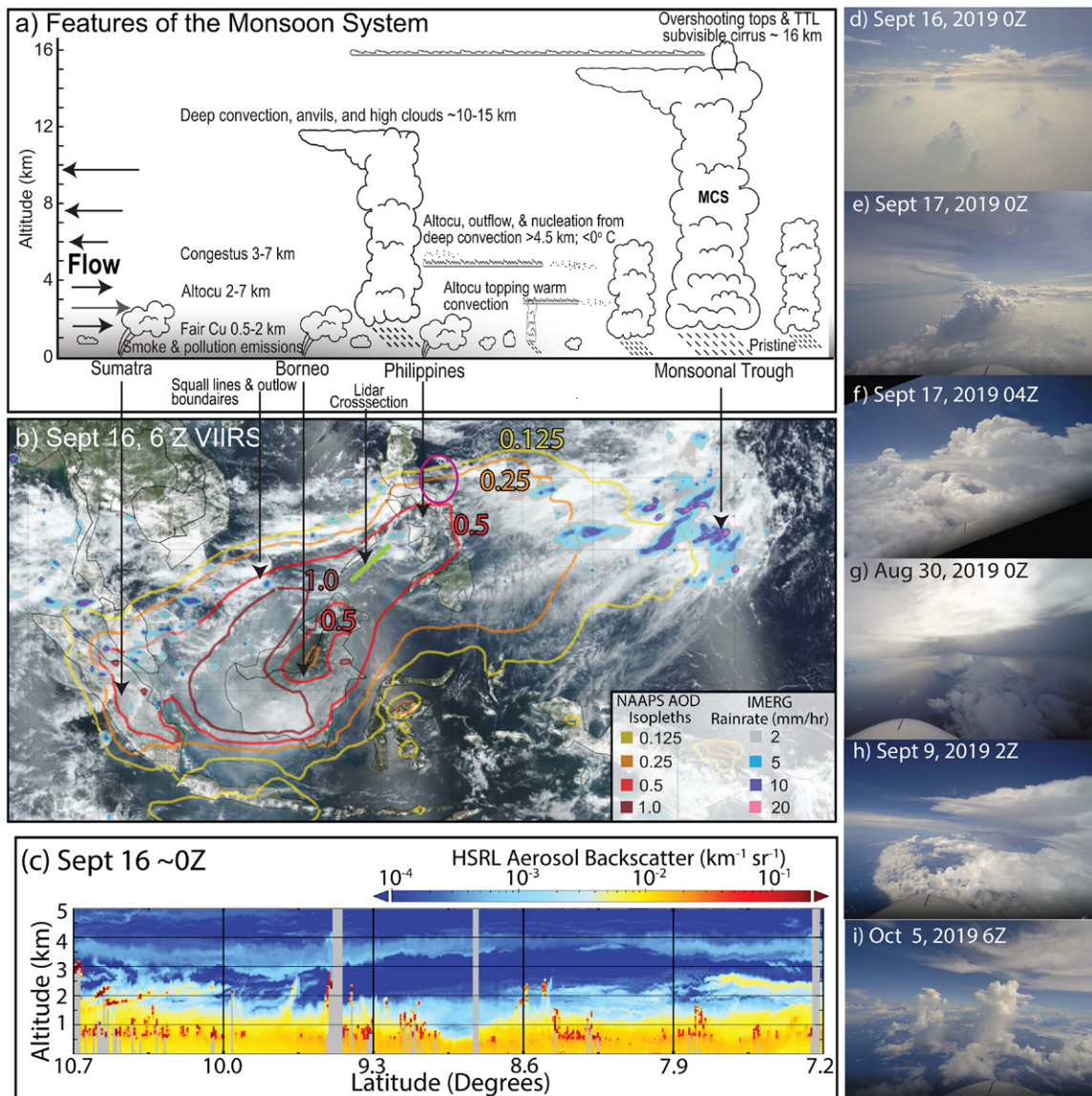
The National Aeronautics and Space Administration (NASA) Cloud, Aerosol and Monsoon Processes Philippines Experiment (CAMP<sup>2</sup>Ex), conducted from Clark International Airport, Philippines, with its 25 August–5 October 2019 intensive operations period, worked to deconvolve interlaced aerosol, cloud, and radiation processes to isolate the role of aerosol particles within Southeast Asia's southeast monsoon system. To document the mission and promote its use to a broad interdisciplinary community, this paper provides a summary of CAMP<sup>2</sup>Ex, a demonstration of some of the technology developed to meet its scientific goals, and the mission's assets, experienced environments, and early scientific findings. To promote the use of CAMP<sup>2</sup>Ex data, extensive supplemental material is also provided for the measured

environment, the instrument payloads/performances, and remote sensing and modeling components (supplemental sections S.1, S.2, and S.3, respectively). CAMP<sup>2</sup>Ex was organized around compositional, convective, and radiative focus areas with associated in situ, modeling, and remote sensing technology efforts investigating warm- and mixed-phase clouds, such as fair weather cumulus, congestus, and altocumulus, as well as their organization and proclivity to develop into deeper convection. NASA's P-3 aircraft, Stratton Park Engineering Company's (SPEC) Learjet 35 aircraft, a Manila Observatory ground site, and partners including the Office of Naval Research (ONR) Propagation of Intraseasonal Tropical Oscillations (PISTON; Sobel et al. 2021) R/V *Sally Ride* research cruise and those involved in the Years of the Maritime Continent (Yoneyama and Zhang 2020), made useful observations. CAMP<sup>2</sup>Ex promoted not only interdisciplinary observations, but new informatics technologies to fuse field observations with satellite remote sensing and modeling efforts to holistically examine the monsoon system. CAMP<sup>2</sup>Ex supports the next generation of Earth-observing systems including a host of the latest geostationary sensors such as on *Himawari-8* (Bessho et al. 2016) and NASA's developing Atmosphere Observing System (AOS).

### **CAMP<sup>2</sup>Ex within the southwest monsoon environment**

Despite broad knowledge of aerosol–cloud relationships, the real-world impact of these processes in the monsoon environment remains highly uncertain (IPCC 2013; National Academies of Sciences, Engineering, and Medicine 2018). Mindanao farmers, for instance, noted a climatic decline in the number of light precipitation days, leading to agricultural stress. At the same time, Philippine urbanization is thought to increase rainfall locally (Cruz et al. 2013; Bagtasa 2020). These observations resulted in a number of climate questions and subsequent studies associated with the 7 Southeast Asian Studies Program (7SEAS; Reid et al. 2013) and led to the formation of the CAMP<sup>2</sup>Ex mission. Aerosol–cloud interactions were one of the hypothesized factors causing precipitation modulation. However, isolating one component of an aerosol–cloud system is confronted by the inherently coupled nature of the aerosol life cycle within meteorological, terrestrial/maritime, cloud, and radiation processes. CAMP<sup>2</sup>Ex met this challenge by isolating biomass burning and anthropogenic emissions life cycles within MC's southwest monsoon (SWM) system. By basing in the Philippines, CAMP<sup>2</sup>Ex observations were located between emissions sources in the MC and sinks within the northwest tropical Pacific (NWTP) monsoonal trough. This placement enabled observations of composition, cloud, and radiation within a host of tropical to subtropical meteorological phenomena in conditions ranging from highly polluted to pristine. Consideration was made for the inhomogeneous nature of the meteorology and composition. Indeed, while the “Maritime Continent” is often thought of as being maritime in nature, in reality the region out to 500 km from shore is often littoral in nature with a combination of both terrestrial and maritime influences.

Figure 1 provides examples of the aerosol and convective elements of the region. Figure 1a provides an overview chart with Fig. 1b depicting a corresponding smoke outbreak matching the overall conceptual model as observed by *Suomi NPP* VIIRS on 16 September 2019 (near the mission's midway point), overlaid with filled contours of satellite-estimated precipitation and open isopleths of 550-nm smoke aerosol optical depth (AOD) from a consensus of models (Sessions et al. 2015; Xian et al. 2019). Smoke from peat fires on Borneo and Sumatra was transported by the SWM flow for over 4,000 km around Borneo, over the Sulu Sea, across the Philippines, and eventually into the mesoscale convective systems (MCSs) within the NWTP monsoonal trough. Aloft, winds reverse in direction becoming northeasterly with the lightest winds at 5 km. On 16 September, the P-3 flew to the north of Borneo in this heavy smoke where AOD at 532 nm was ~1. The vertical profiles of aerosol backscatter shown in Fig. 1c were measured by lidar (track marked by a green line in Fig. 1b), with aerosol layers (here predominantly smoke) depicted as warmer colors with clouds as red. Visual context



**Fig. 1. Aerosol and cloud phenomena of the southwest monsoon system.** (a) Overview of the monsoonal system from the Maritime Continent through the Philippines to the western Pacific monsoonal trough. (b) A corresponding SNPP VIIRS image to (a) of a typical smoke event (16 Sep 2019) with overlaid Integrated Multi-satellite Retrievals for GPM-IMERG satellite precipitation rates (Tan et al. 2019; Huffman et al. 2020) and open isopleths of 550-nm smoke aerosol optical depth (AOD) from the Navy Aerosol Analysis and Precision System Reanalysis (NAAPS; Lynch et al. 2016) showing transport of smoke 4,000km from Borneo into mesoscale convective systems in the monsoonal trough. (c) High Spectral Resolution Lidar 2 (HSRL-2; Burton et al. 2016) aerosol backscatter over the Sulu Sea on this day along the track marked in green on (b); (d) eastward view from cockpit at the southernmost point of (c); (e) convergence line of convection from the same plume over the NWTP the following day (17 Sep 2019); and (f) edge of a nearby MCS terminating the plume (17 Sep 2019). Other aerosol convective feature interactions included (g) coastal convection spawned by a morning land breeze, (h) isolated convective cell with forming cold pool, and (i) congestus in pristine conditions on the very last flight of the mission.

for this time is provided in Fig. 1d. With most of the smoke below 1-km altitude, visibility in the marine boundary layer (MBL) was only a few kilometers and mass concentrations neared  $100 \mu\text{g m}^{-3}$  even though the location was 2,000 km downwind from the source. Most MBL clouds were only a few hundred meters deep, but congestus had tops to 3 km with sporadic altocumulus. Additional cloud-lofted aerosol layers between 2 and 5 km were also observed. The following day (17 September 2019), the P-3 sampled the smoke again, this time over the NWTP after an additional day of transport (marked as a magenta oval in Fig. 1b). Over the NWTP, convergence/confluence lines of convection developed within the smoke

with cloud-top heights to 3–4 km (Fig. 1e) as well as sharp boundaries of smoke and organized deep convection and squall lines (Fig. 1f). In addition to sampling such massively polluted environments as this, CAMP<sup>2</sup>Ex sampled a host of low- to midlevel convective entities, including land–sea breeze fronts and induced deep convection with tops to 14+ km (Fig. 1g); convection developing into deep phases to 14+ km and spawning strong cold pools (Fig. 1h); significant particle removal by organized systems in the monsoonal trough (Fig. 1i); and a wide variety of fair weather cumulus, congestus, and altocumulus in both pristine and polluted conditions (Fig. 1j). Such sampling was performed in a range of pristine to Asian mainland and polluted environments. All of these features in Fig. 1 had strong relationships to the overarching thermodynamic environment. Corresponding skew-*T* and visible satellite imagery is provided in section S.1 of the online supplemental material.

Notable in Fig. 1 are complex trilevel cloud formations (Johnson et al. 1999) including near ever-present cirrus (including subvisible cirrus) and altocumulus (e.g., Sassen and Wang 2012) that impact both solar and terrestrial radiation budgets. Further, embedded in the coupled system is a daunting number of multiscale drumbeats of the interseasonal oscillations such as El Niño–Southern Oscillation (ENSO), the monsoon (Chang et al. 2005), and the Madden–Julian oscillation (MJO)/boreal summer intraseasonal oscillation (BSISO; Jiang et al. 2004; Zhang 2005; Reid et al. 2012) down to various convective entities such as tropical cyclones and MCSs (supplemental section S.1). At the finest scales are diurnal radiation and air–sea–land contrasts that influence air–sea fluxes (e.g., Fairall et al. 1996a,b; Clayson and Bogdanoff 2013), the MBL (e.g., de Szoeke et al. 2021), and the sea–land breeze (Qian 2008; Qian et al. 2010; Wang et al. 2013). Indeed, these in turn modulate low clouds, congestus, and deep convection (Matsui et al. 2006; Ruppert 2016) with feedbacks to precipitation (e.g., Li et al. 2010; Yang and Smith 2008; Ruppert and Johnson 2015; Minobe et al. 2020). Such phenomena are tightly intertwined with aerosol emissions and life cycle (Nichol 1998; Reid et al. 2012, 2015, 2016b,a; Wang et al. 2013), aerosol transformations (Atwood et al. 2017), and aerosol scavenging (Xian et al. 2013). Aerosol–cloud interactions may also feed back into measurement assumptions and biases in the very same instruments used to monitor them (e.g., rationale for Saleeby et al. 2010).

### **CAMP<sup>2</sup>Ex focus areas**

CAMP<sup>2</sup>Ex was organized around the focus areas of composition, clouds, and radiation that contributed to Philippine air quality and convection priorities. Integrating these components was an overarching technology effort to provide context to the observations as well as supporting a series of ongoing cross-disciplinary studies, including refinement of remote sensing retrievals, modeling, and informatics technologies.

**Composition.** This focus area quantified air mass composition, aerosol optical and microphysical properties [e.g., size, hygroscopicity, cloud condensation nuclei (CCN) efficiency, absorption], and the overall aerosol life cycle of sources, transport, transformation, nucleation, and sinks. The community needs to know which particles activate as cloud droplets or remain as interstitial particles; we also need to know which processes affect particle transformation, detrainment aloft, and removal by precipitation. Investigations focused on particle evolution including scavenging, cloud processing, and nucleation feedbacks onto CCN budgets. To improve aerosol monitoring and modeling, and to investigate fundamental particle observability, a significant effort is being made to infer aerosol microphysical properties from remote sensing observations, in particular, polarimeters, lidars, and imagers. CAMP<sup>2</sup>Ex continues to assess and advance remote sensing retrieval algorithms that quantify important geophysical aerosol parameters such as CCN concentration, aerosol “type,” or “chemical speciation” from remote sensing.

**Cloud physics.** The cloud physics focus area tested specific hypotheses about aerosol impacts on cloud microphysics and precipitation. More polluted conditions are thought to increase cloud droplet number and reduce cloud droplet size, but reduce raindrop number and increase mean raindrop size (Altaratz et al. 2008; Saleeby et al. 2010; May et al. 2011; Sheffield et al. 2015), with corresponding increases in overall congestus height (Konwar et al. 2012; Li et al. 2013; Sheffield et al. 2015). The strength of this impact may be modulated by environmental factors such as wind shear, relative humidity, and convective available potential energy (CAPE; e.g., Lee et al. 2008; Khain et al. 2008; Storer et al. 2010, 2014; S. Freeman et al. 2023, unpublished manuscript). Dynamical feedbacks between aerosol and cloud processes are also being examined such as whether increases in CCN weaken cold pools (e.g., supporting studies of Saleeby et al. 2010; Storer et al. 2010; Grant and van den Heever, 2015; dissenting studies of Tao et al. 2007; Cotton et al. 2012). Finally, this focus area also worked to evaluate detrainment processes of aerosol particles and water vapor (Leung and van den Heever 2022), as well as their precursors into the free troposphere and their association with altocumulus cloud life cycle.

**Radiation and energy budget.** The cloud and aerosol system is also forced by diurnally varying radiation. Atmospheric radiation is not only a strong forcing agent for the system, but also a primary means for monitoring aerosol and cloud properties by remote sensing. Objectives include the quantification of the diurnal radiation budget in complex maritime tropical cloud fields, including the role of cirrus and altocumulus in convective cloud development. From a remote sensing perspective, resolved and unresolved cloud heterogeneities were investigated to characterize their impact on cloud property retrievals. Technology developments for advancing the remote sensing of cloud properties include cloud stereography, tomography, convolutional neural network (CNN) retrievals, along with methods to constrain 3D radiation fields and cirrus properties above the aircraft or at surface sites.

Within these focus areas, the Manila Observatory (MO) led further Philippine efforts focused on local and long-range transport of pollutants (e.g., Cruz et al. 2019; Braun et al. 2020; Hilario et al. 2020) and on the confounding relationships between aerosol emissions and land use change on convection. Monitoring at MO allows studies in these focus areas to occur within highly urbanized environments, including investigating how diurnal urban boundary layer characteristics are related to cloud and radiation environments, and ultimately to air quality.

### **Mission design and assets**

CAMP<sup>2</sup>Ex planning accounted for the many scales associated with the monsoonal system. During the June–September SWM, low-level winds advect aerosol emissions from Indonesia, Malaysia, and Singapore, in their climatological dry and fire-prone period, toward the NWTP (e.g., Fig. 1a; Xian et al. 2013). After the late September–October SWM transition, the reverse flow occurs to form the northeast monsoon (NEM); a monsoon trough develops over the Indian Ocean, Sumatra, and Borneo, and the NWTP transforms into a drier phase. Figure 2 provides an overview of the regional monsoonal environment divided into late SWM 24 August–22 September 2019 (Fig. 2a) and early NEM 23 September–5 October 2019 (Fig. 2b) mission sampled study periods. During the SWM period, MC emissions were carried by the low-level southwest winds through the Celebes, Sulu, and South China Seas, and eventually into the larger convective elements associated with the NTWP monsoon trough. Throughout this period, the BSISO constantly marched across the region while a steady stream of tropical disturbances and cyclones formed in the NWTP and propagated to the northwest over and to the north of Luzon. These multiscale convective processes resulted in a series of monsoon enhancements and aerosol transport events from Borneo (supplemental section S.1). After an abrupt change from the SWM to the NEM on 21–23 September 2019, regional transport

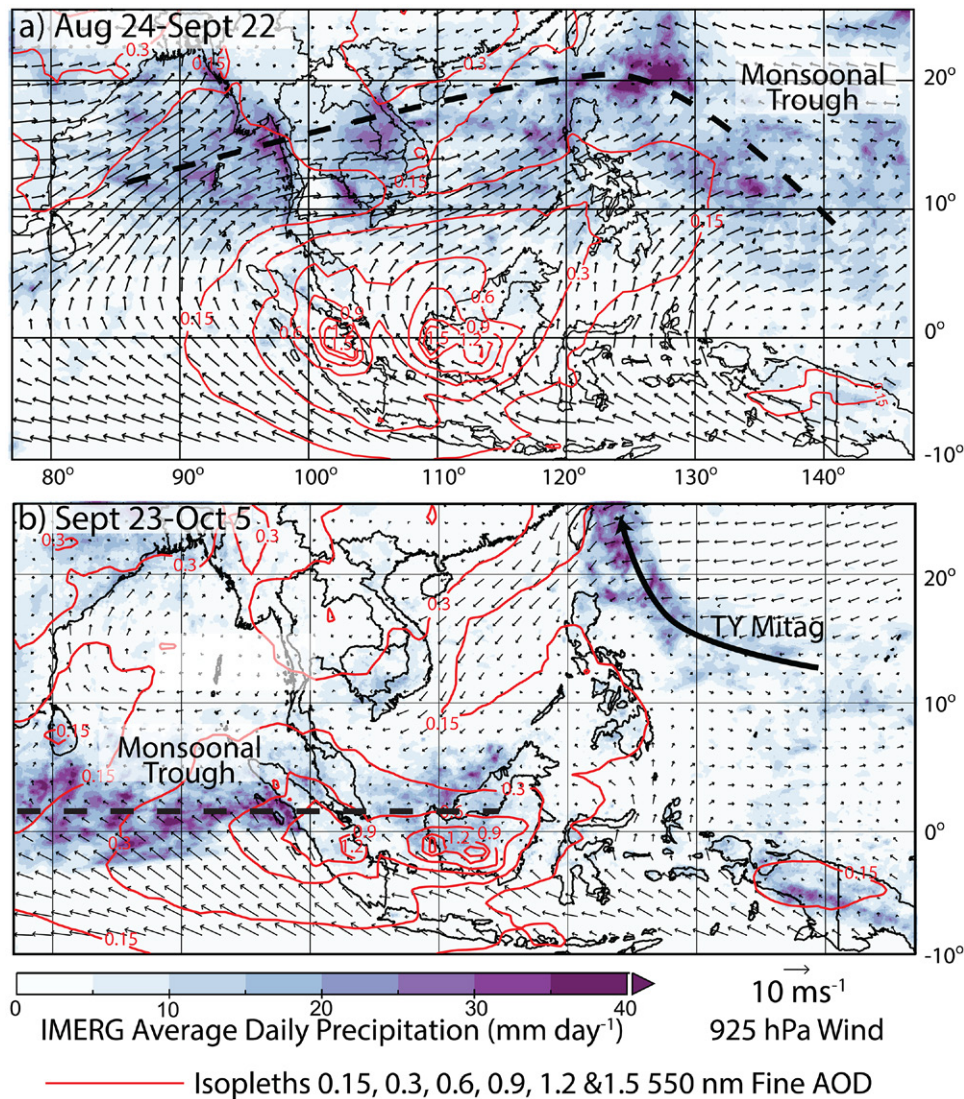


Fig. 2. An overview of the regional monsoonal environment during the CAMP<sup>2</sup>Ex airborne operations period into (a) late SWM during 24 Aug–22 Sep 2019 and (b) early NEM sampled 23 Sep–5 Oct 2019. Included are mean 925-hPa winds from the ECMWF Reanalysis v5 (ERA5; Hersbach et al. 2020), satellite precipitation from IMERG, and fine-mode AOD from the International Cooperative for Aerosol Prediction consensus of the world’s operational global aerosol models (ICAP-MME; Xian et al. 2019). Monsoonal troughs, marked by heavy dashed lines, were analyzed by their surface pressure minimums. Also noted in (b) is the location of the period precipitation maximums over the NWTP due to the propagations of Typhoon Mitag.

became less organized, the region hosted considerably less cirrus, and a variety of Asian pollution sources interspersed with NWTP air. Thus, conditions ranged from pristine to long-lasting emissions originally advected during the SWM. While considerably drier than earlier periods, tropical cyclones were still active in the region, as evidenced by the precipitation maximum in Fig. 2b east of Taiwan owing to the life cycle of Typhoon (TY) Mitag.

**Flight operations and mission instrumentation.** Given the complexity and spatial inhomogeneity of the MCs meteorology, the overall mission strategy was to rely heavily on airborne and space-based remote sensing for cloud and aerosol characterization, with in situ observations informing the skill and improvements of retrievals, and models providing large-scale context. The NASA P-3 conducted 12 SWM and 7 NEM flights for a total of 148 h over a host of meteorological conditions that can project back onto remote sensing. The SPEC Learjet 35 focused on deeper convection—especially in conjunction with P-3 and R/V *Sally Ride* remote



sensors, with 10 SWM and 3 NEM flights for 37 h. P-3 flight tracks and key site locations are provided in Fig. 3a with a mission calendar and instrumentation provided in supplemental sections S.1 and S.2, respectively. With the P-3's endurance of ~9 h and ceiling of ~6–8 km (depending on fuel load), the operations area ranged from the southern Sulu Sea to sample the air as it exited Borneo, to the NNE of Luzon to sample pristine NWTP environments. The PISTON R/V *Sally Ride* was stationed ~700 km to the east of Manila from 5 to 25 September and marked the approximate eastern operations extent. The SPEC Learjet 35, with a 4-h endurance but greater airspeed and maximum altitude of 13 km, was tasked to provide more measurements of active convection already being sampled by the P-3, or monitored from the R/V *Sally Ride*.

An accounting of atmospheric instruments deployed on the P-3, Learjet 35, and at the Manila Observatory along with the location of key instruments of PISTON's R/V *Sally Ride* are shown in Figs. 3b–e, respectively. CAMP<sup>2</sup>Ex depended heavily on the P-3's remote sensing and profiling observations for monitoring the evolution of aerosol and cloud structure (supplemental Table S.2.1). Typically, the P-3 would arrive to survey a target region at maximum altitude (~6–8 km). The active two-wavelength extinction (355 and 532 nm) and three-wavelength backscatter (adding 1,064 nm) “2 $\alpha$ -3 $\beta$ ” High Spectral Resolution lidar (HSRL-2; Fig. 1b) on the P-3 provided below-aircraft profiles of spectral light extinction,



Fig. 3. Flight tracks and instrumentation. (a) Flight tracks for 19 NASA P-3 flights conducted between 25 Aug and 5 Oct 2019. Also noted is the Clark airborne base of operations and the operations area of PISTON's R/V *Sally Ride* collection; (b)–(e) Key P-3, SPEC Learjet 35, Manila Observatory, and R/V *Sally Ride* instrumentation, respectively. AERONET = Aerosol Robotic Network; AMPR = Advanced Microwave Precipitation Radiometer; APR3 = Airborne Precipitation Radar 3rd generation; DLH = Diode Laser Hygrometer; HSRL = High Spectral Resolution Lidar; RSP = Research Scanning Polarimeter.

backscatter, lidar ratio (the ratio of particle extinction to backscatter), and depolarization. These quantities can be further related to aerosol type and particle size, cloud-top heights, and boundary layer structure. The passive Research Scanning Polarimeter (RSP) retrieved cloud optical thickness, cloud-top height, droplet and aerosol particle size distributions, aerosol optical depth, aerosol absorption, and aerosol refractive index. Its multiangle polarimetric observations that use parallax and cloud bow structure are resistant to the influences of the ubiquitous thin cirrus above (Alexandrov et al. 2012a). The Airborne Third Generation Precipitation Radar (APR3) Doppler Ka-, Ku-, and W-band radar and the four-band Advanced Microwave Precipitation Radiometer (AMPR) provided profile and integrated information on cloud liquid/ice water, precipitation rates, and drop size. Full-frame broadband mid- and longwave imagery, as well zenith and nadir all-sky cameras, provided parallax information on cloud topography. Finally, dropsondes provided state profiles to combine with profiling remote sensors, thereby providing environmental context of these measurements.

P-3 remote sensing was supported by in situ measurements including measurements of meteorological state and 20-Hz turbulence and water vapor (supplemental Table S.2.2). Radiation measurements included upwelling and downwelling total solar, total longwave, and hyperspectral solar, in conjunction with downwelling direct and diffuse broadband (400–2,700 nm) and spectral (350–1,000 nm at 1-nm resolution) solar radiation. These helped constrain the radiative budget and assess heating rates, and also allowed for estimation of cirrus and aerosol optical depth. Aerosol particle, droplet, and ice size measurements spanned 10 nm to millimeters, with internal (from NASA/Washington University) and wing-mounted (from SPEC Inc.) probes. A comprehensive NASA Langley Aerosol Research Group Experiment (LARGE) and gas chemistry package was installed for particle microphysics, optical properties, and chemistry. A particularly unique capability of the P-3's in situ package was the measurement of cloud droplet chemistry.

The SPEC Learjet 35 was equipped with in situ probes to characterize active convection from cloud base to top, especially for clouds penetrating above the P-3's ceiling (Fig. 2c; supplemental Table S.2.5). Included were state, liquid/ice water, and microphysics probes to characterize cloud cores, precipitation, and ice formation. These included overlapping ranges of sampling sizes from aerosol condensation nuclei (CN) and fine-mode size to small cloud droplets and precipitation, as well as droplet and ice crystal imaging. Identical instruments were included on the P-3 when possible. For airborne coordination, early in the mission the Learjet 35 operated in the same region as the P-3. By the mission midpoint, the Learjet 35 flew below the P-3, providing in situ observations that corresponded to the P-3's remote sensors.

To provide context to the airborne mission, a 2018 through early 2020 CAMP<sup>2</sup>Ex Weather and Composition Monitoring (CHECSM) effort was initiated, centered on sensors located at the Manila Observatory that monitored aerosol, cloud, and radiation properties within the Metro Manila megacity. CHECSM provides a framework to evaluate satellite and model products, assess regional weather and climate, and evaluate local, maritime, and long-range transport contributions to the Manila region. In this way, CHECSM afforded an avenue to engage local agencies and students in a manner that projected both onto CAMP<sup>2</sup>Ex science requirements and applications important to the Philippine people—notably air quality and precipitation. The Manila Observatory supported long-term aerosol and radiation monitoring at a megacity with a regional population of over 20 million. At the center were a ground-based HSRL to monitor aerosol and cloud layers, and radiometers to close the radiative budget at the surface, including solar, IR, and direct/diffuse radiation. Extensive surface sampling of aerosol properties was conducted including size-resolved aerosol chemistry and black carbon to support air quality studies (e.g., Cruz et al. 2019; Braun et al. 2020; Stahl et al. 2020; Hilario et al. 2020).

PISTON's 2019 R/V *Sally Ride* cruise provided continuous measurements of the troposphere, ocean, and air–sea transition zone including a bulk and direct flux measurement

package and a comprehensive set of atmospheric and oceanographic profiling sensors (Sobel et al. 2021; data access and full data description: <https://www-air.larc.nasa.gov/cgi-bin/ArcView/camp2ex?RV-SALLY-RIDE=1>). PISTON also included a nearly equivalent ship cruise in 2018 on R/V *Thomas G. Thompson*, an array of profiling ocean floats, and two full-depth ocean moorings (data at aforementioned website under different tabs). Atmospheric remote sensing of clouds and air motion that support collaboration with CAMP<sup>2</sup>Ex include the SEA-POL C-band (Rutledge et al. 2019) and NOAA W-band radars (Moran et al. 2012), wind and HSRL lidars, and 3-hourly radiosondes. The P-3 and Learjet 35 had three and five flights, respectively, characterizing the environment around the *Sally Ride*.

**Remote sensing, modeling, and environmental informatics.** Mission operations and analysis required the integration of a multitude of product types (see supplemental section S.3 for more remote sensing, modeling, and informatics details). CAMP<sup>2</sup>Ex makes full use of and supports the global meteorological constellation of optical, radar, microwave, and scatterometer products. Of paramount importance was the cooperation of the Japan Meteorological Agency (JMA) for expedited Advanced Himawari Imager (AHI) data access, as well as the acquisition of 2.5-min rapid scan data. The Japan Amazon Web Services node provided imagery and products at 15-min latency for integrating into real-time flight operations. Cloud and aerosol products were derived from this dataset by porting algorithms from NASA MODIS.

CAMP<sup>2</sup>Ex supports the development of next-generation satellite products, including new geostationary algorithms, optical flow algorithms, aerosol and cloud polarimetric remote sensing for NASA's upcoming Plankton, Aerosol, Cloud, Ocean Ecosystem (PACE) and AOS missions, and the ESA Aeolus wind lidar (supplemental section S.3.1). Of great value to CAMP<sup>2</sup>Ex was its application of high-resolution imagery, typically only acquired over land, to study maritime cloud properties and evaluate issues due to the relatively coarse resolution of existing satellite-based instruments typically used for atmospheric remote sensing. CAMP<sup>2</sup>Ex was granted large acquisitions of ASTER, *Landsat-8*, and Sentinel-2 within ~800 km of the Philippine coasts. Multiview digital globe high-resolution imagery was also ordered, including stereographic views.

Modeling efforts in support of CAMP<sup>2</sup>Ex were also diverse. CAMP<sup>2</sup>Ex forecasting relied heavily on the Met Office; Philippine Atmospheric, Geophysical and Astronomical Services Administration (PAGASA); European Centre for Medium-Range Weather Forecasts (ECMWF); and Joint Typhoon Warning Center (JTWC) forecasting and data, as well as aerosol predictions from the U.S. Naval Research Laboratory (NRL), NASA's Global Modeling and Assimilation Office (GMAO), and other International Cooperative for Aerosol Prediction ICAP consensus members (Sessions et al. 2015; Xian et al. 2019). The rapid evolution of convection around the Philippines, and at the airfield in particular, required monitoring of PAGASA's radar network. Post-mission analysis has spanned a range of scales and models. Of particular use are a series of basin-scale mesoscale-resolution simulations of the entire Maritime Continent, flight-specific mesoscale-resolution, and large-eddy simulations (LES) all using the Regional Atmospheric Modeling System (RAMS; Cotton et al. 2003; Saleeby and van den Heever 2013) at Colorado State University, as well as global reanalyses at GMAO and NRL. Each modeling effort focuses on different problems, ranging from interactions within the large-scale meteorological system to aerosol, microphysical, and dynamical processes within individual clouds.

Integrating observations, satellite, and modeling data has been a series of informatics efforts. Data are made available to the public not only through the CAMP<sup>2</sup>Ex project DOI landing page (<https://doi.org/10.5067/Suborbital/CAMP2EX2018/DATA001>) hosted at NASA Atmospheric Science Data Center, but also via two visualization websites. JPL applied the Hurricane Watch Package to the CAMP<sup>2</sup>Ex domain where, to provide regional environmental context,

satellite, model, and a subset of aircraft observations can be overlaid and downloaded (<https://camp2ex.jpl.nasa.gov/>; last accessed: March 2022; Hristova-Veleva et al. 2020). The University of Wisconsin ported NASA Worldview to focus on even higher-temporal-resolution geostationary applications to the aircraft and *Sally Ride* (<http://geoworldview.ssec.wisc.edu>; last accessed: March 2022). To help introduce data users to the CAMP<sup>2</sup>Ex P-3 dataset, the University of Illinois created a full flight data fusion dashboard for a single flight (16 September 2019) where all instruments can be monitored (Di Girolamo et al. 2021; [https://viridir.ncsa.illinois.edu/NCSAvis/camp2ex/public/deliverables\\_6-15-21/](https://viridir.ncsa.illinois.edu/NCSAvis/camp2ex/public/deliverables_6-15-21/)). All of these tools are designed to allow the broader community to engage with CAMP<sup>2</sup>Ex and PISTON science.

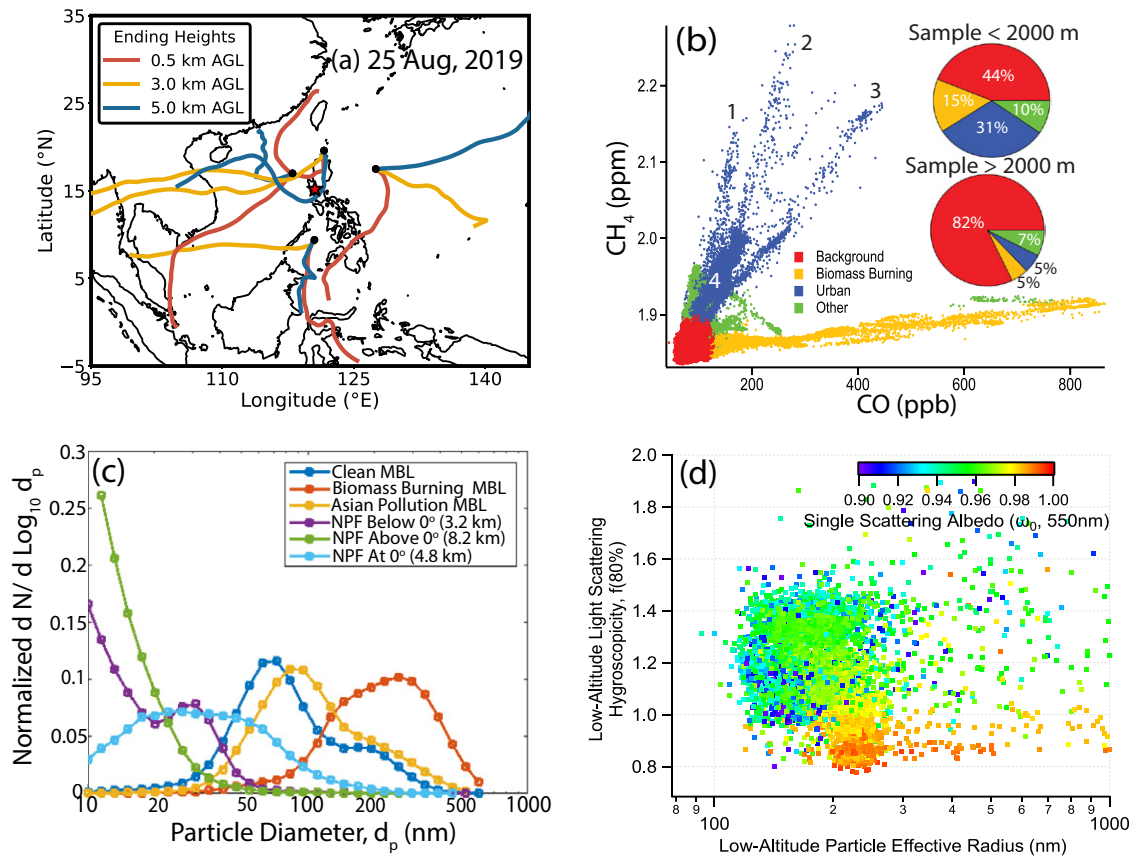
### **Observations of the coupled system**

The 2019 season provided excellent conditions with above-average biomass burning emissions, the frequent influence of tropical disturbances, and an early monsoon transition (supplemental section S.1). These led to a wide dynamic range of environments being sampled for all focus areas.

**The compositional environment.** While much can be learned from remote sensing and modeling of aerosol life cycle, large uncertainties remain in fine vertical features, air mass histories, evolving aerosol properties, and ultimately small-scale processes. While curtain data such as those in Fig. 1b provide excellent detail on layers and some information on aerosol size, they must nevertheless be combined with other information to address science and monitoring needs, including: What is the dominant particle source on average or in a particular air mass? How are particle optical properties that are the basis for remote sensing related to their physical, thermodynamic, and cloud nucleating properties? And how do evolutionary processes change these relationships?

Along flight tracks, CAMP<sup>2</sup>Ex utilized a combination of back-trajectory modeling and trace-gas analysis to classify aerosol sources. Trajectory modeling along every point throughout a flight track was a crucial first step as directional wind shear often resulted in different source regions along the vertical profile within the operations area (e.g., Fig. 4a; Hilario et al. 2021). Because the CAMP<sup>2</sup>Ex domain was so large and CO<sub>2</sub> varied due to biological activity, excess CO and CH<sub>4</sub> (Fig. 4b) were the best in situ tracers for aerosol sources. While both species are products of biomass burning and industrial emissions (Helfter et al. 2016; Nara et al. 2017) and have lifetimes from months to years, low excess CH<sub>4</sub> to CO ratio indicates biomass burning sources (e.g., Akagi et al. 2011). Higher CH<sub>4</sub>:CO ratios were predominantly from anthropogenic sources ranging from peninsular Southeast Asia to East Asia, with local urban sources and Metro Manila among the highest CH<sub>4</sub> values—perhaps due to propane leaks and fuel evaporation. Low CO mixing ratios (<100 ppb) were representative of cleaner marine environments. More reactive gasses and their reaction products, such as SO<sub>2</sub>, NO, NO<sub>2</sub>, NO<sub>x</sub>, and O<sub>3</sub> enable further assessment of sources and photochemical activity.

Dry particle size distributions and chemical composition differ substantially by source, with further modification by chemical and cloud processing (Fig. 4c). Aerosol particles in MC air masses had vastly different modal diameters and distribution shapes on any given day, often with sharp spatial gradients (Fig. 4b). Since CCN concentration is largely a function of the number size distribution, characterizing particle size characteristics was a high mission priority. Fine particles from Borneo biomass burning emissions were relatively large in size, consistent with both smoldering combustion and high concentration-induced coagulation (Reid et al. 2005). In comparison, Asian pollution particles were smaller and indicative of high temperature combustion. The smallest fine-mode aerosol particles were found in the “clean” marine boundary layer along with an enhanced sea salt coarse mode. Deviations from an idealized lognormal distribution (e.g., observed shoulders) can be a result of cloud



**Fig. 4.** Airmass compositional characteristics measured during CAMP<sup>2</sup>Ex. (a) Back trajectories at 500, 3,000, and 5,000 m from the first day of the campaign for four operations quadrants. (b) Airmass typing during CAMP<sup>2</sup>Ex using in situ observations of methane (CH<sub>4</sub>) and carbon monoxide (CO). Inset pie charts show the percentage of observations for low- and high-altitude measurements (i.e., GPS altitude less than and greater than 2.0 km, respectively), excluding observations during takeoffs and landings). (c) Particle mobility derived particle number distributions normalized to total count for some example regimes. (d) Scatterplot light scattering hygroscopicity (the ratio of 80% RH light scattering to dry light scattering from two nephelometers) vs optical-particle-counter-derived effective radius, color coded by single scattering albedo. Evaluating the entire figure, biomass burning smoke from the Maritime Continent was largely from peat fires, leading to very large sizes but higher single scattering albedo and lower hygroscopicity. Pollution particles from East Asia were also large but with higher hygroscopicity owing to increased sulfate fractions. Clean marine particles were smaller, due to a lack of anthropogenic sources and particle scavenging. Smallest particle sizes were associated with new particle formation (NPF) events. Note in all cases, particle distributions deviate from idealized lognormal behavior—a likely outcome from particle production and scavenging mechanisms.

processing (e.g., Hoppel et al. 1986) or may indicate multiple sources or scavenging along the transport pathways. For example, “clean marine” fine particles could be generated by marine sources, but can also be dominated by long-lived residuals from terrestrial source particles (Clarke et al. 1996; Quinn et al. 2017). Photochemically generated New Particle Formation (NPF; Wang et al. 2017, 2018) events were frequently observed where large numbers of 1–10-nm-sized particles nucleate from precursor gases in detraining cloud layers—often at or above the 0°C/4.8-km melting level (Xiao et al. 2023; Reid et al. 2019). To help close the overall CCN budget and determine which chemical species are dominating cloud composition, cloud water chemistry was analyzed and showed a significant contribution from sea salt even in polluted cases where it was modulated by industrial and biomass burning emissions (Stahl et al. 2021).

Measurements of aerosol size, when coupled with knowledge of composition including light absorbers like black carbon or hygroscopic species like sulfate, allow for a better accounting

of particle-driven radiative perturbations, heating rates, thermodynamic properties, and air quality. Commensurate with the variability in aerosol sources, processing, and resulting size, aerosol particles likewise showed significant variability in chemical, thermodynamic, and optical properties (Fig. 4d). Full closure of optical and thermodynamic properties continues as we suspect difficult-to-characterize semivolatile aerosol components are at work, and current estimates of key optical and thermodynamic properties should be taken as semi-quantitative. However, there was generally distinct diversity between aerosol populations. Aged biomass burning particles, dominated by particulate organic matter, were distinct with generally larger dry effective radius and low hygroscopicity, and low absorption leading to high single scattering albedo owing to the largely smoldering peat fire sources. Previous measurements suggest peat smoke to be hygroscopic including higher inorganic fractions than smoke from other regions (e.g., review by Reid et al. 2013). However, CAMP<sup>2</sup>Ex found lower-than-expected hygroscopic growth factors for aged biomass burning particles that have a composition dominated by organic mass. While aggregate chain restructuring (i.e., collapsing to more spherical shapes) has been used to explain sub-1  $f(\text{RH})$  values previously for less aged biomass burning observations (Shingler et al. 2016) the highly coated nature of aged Borneo smoke makes this explanation less plausible. Losses of semivolatile material, differential losses of particles in the humidification system, or volatilization losses due to aqueous processing could all contribute to a low bias of  $f(\text{RH})$  measurements, but more work is needed to elucidate the true cause of this unique phenomenon. Anthropogenic combustion sources produced smaller particles, but each source had its own character; for example, Manila yielded larger amounts of light absorbing black carbon and nonhygroscopic organics, while particles from Asia were more hygroscopic with high sulfate mass fractions. Given the diversity of aerosol sources in the region, mixtures and processed particles could have properties anywhere in between.

**Convection.** Characterization of aerosol particle properties enables CAMP<sup>2</sup>Ex investigators to evaluate cloud hypotheses related to aerosol effects on cloud height, droplet/precipitation effects, and cold pools. The effect of aerosol particles on cloud water and height distribution is particularly illustrative of the aerosol–cloud microphysics relationship studied. The P-3's HSRL-2 lidar easily distinguished between clean and polluted conditions. The APR-3 Ka-, Ku-, and W-band radars coupled with the AMPR microwave radiometer provided information on cloud water and precipitation. The CCN environment around clouds were often based on HSRL measured 532-nm AODs, which spanned pristine 0.05 to highly polluted environments over 1. Aerosol environments were subsequently categorized into terciles of AOD delineated by  $<0.12$  (clean marine) and  $>0.2$  (polluted conditions; consistent with Ross et al. 2018). The role of the thermodynamic environment in modulating such aerosol responses was assessed using the dropsondes. Figures 5a and 5b show contoured frequency by altitude diagrams of W-band radar reflectivity for clouds in the upper and lower terciles of AOD, respectively. The differences in the distributions are obvious: the high-AOD tercile has a greater frequency of cloud tops between 2 and 3 km while the low-AOD indicates only sporadic observations of cloud top above 2 km. The high-AOD clouds also have a significantly different vertical weighting of W-band reflectivity, with a tendency for the observed reflectivity that is not corrected for attenuation in these plots to be weighted much nearer to cloud top and with a greater proportion of values above 0 dBZ in the high-AOD cases. A common feature in both CFADs is the tail of high reflectivity extending from 3 to 5 km due to precipitating altocumulus, a very common occurrence in this region. AMPR 85- and 37-GHz brightness temperatures are plotted in Figs. 5c and 5d and show increased temperatures for more polluted environments suggestive of higher liquid water paths. These early CAMP<sup>2</sup>Ex results are consistent with aerosol-induced invigoration of shallow cumulus.

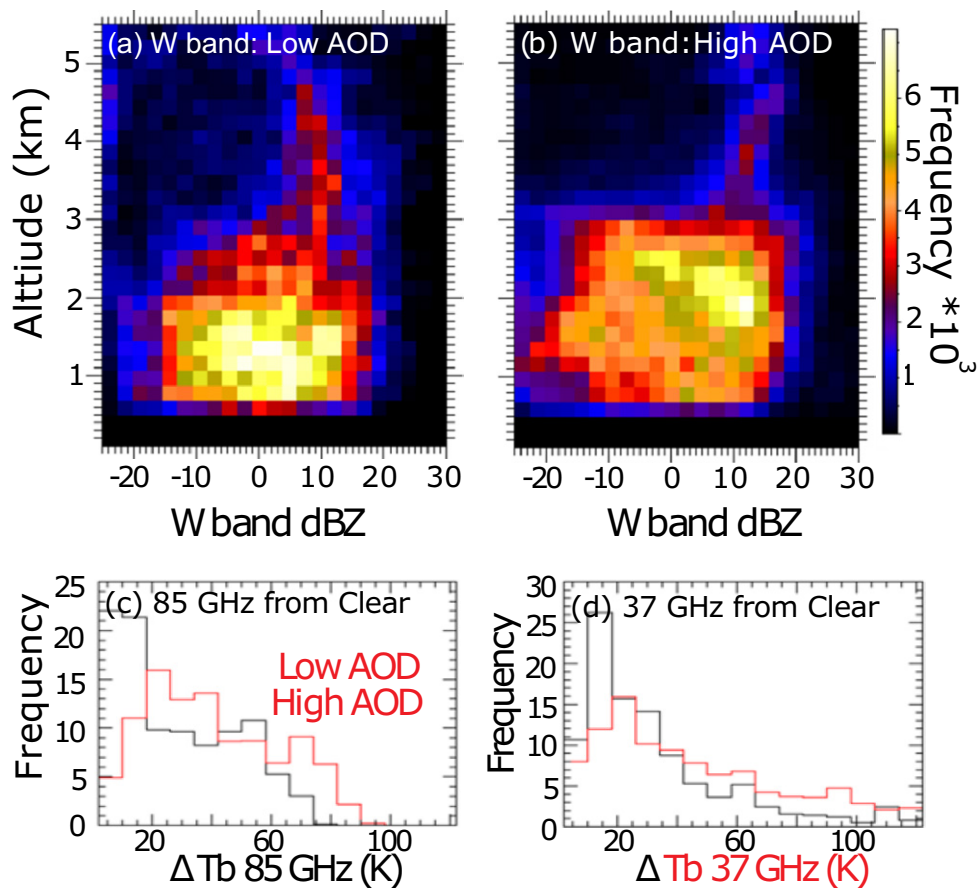


Fig. 5. (a),(b) Frequency by altitude diagrams of radar reflectivity from the APR-3's W-band radar. The low-AOD plot in (a) shows clouds that are matched with a 532-nm AOD measured by HSRL-2, which is in the lower tercile of AODs ( $<0.12$ ) measured across the campaign. These can be considered "baseline" clouds in pristine environments. The high-AOD plot in (b) shows clouds that are matched with AODs in the upper tercile ( $>0.2$ ). Note that the clouds are deeper and have strong reflectivity (i.e., water content) toward the top; this is supported by distributions of (c) 85- and (d) 37-GHz microwave brightness temperature differences between cloud and nearby clear-sky measured by AMPR are shown for the low-AOD and high-AOD conditions, respectively.

These observations of bulk aerosol and cloud properties were then linked to observed drop microphysics. Clues exist in systematic height dependence in droplet size for both in situ observations and the P-3's Research Scanning Polarimeter (RSP) cloud retrievals. Figure 6a shows a "rainbow plot" of 70 droplet size distributions (DSDs) for submillimeter diameter droplets in ice-free updrafts collected by the Learjet 35 and averaged over  $2^{\circ}\text{C}$  intervals. The concentration of small drops decreased and large drop sizes commensurately increased in the tail of the distribution with decreasing temperature, i.e., increasing cloud height. These distributions are summarized in temperature dependencies in measured droplet number concentrations (Fig. 6b) and droplet effective radius (Fig. 6c). CAMP<sup>2</sup>Ex observations are consistent with previous observations of a correlation between DSD  $r_{\text{eff}}$  and coalescence processes as cloud drops ascend in an updraft (e.g., Andreae et al. 2004; Freud and Rosenfeld 2012). The current consensus suggests active coalescence exists when  $r_{\text{eff}}$  reaches a value of 12–14  $\mu\text{m}$ . This finding can be applied to remote sensors, most notably RSP's rainbow Fourier transform technique that can provide DSD retrievals below 100- $\mu\text{m}$  radius (Alexandrov et al. 2012b). Figures 6d and 6e provide direct comparisons of Learjet 35 cloud-top DSD and corresponding P-3 RSP retrieved distributions during coordinated flights, demonstrating remarkably good skill in replicating temperature–DSD relationships. Despite RSP's insensitivity to the largest drops, polarimetry can indicate the occurrence of coalescence. Indeed, Fig. 6f illustrates the

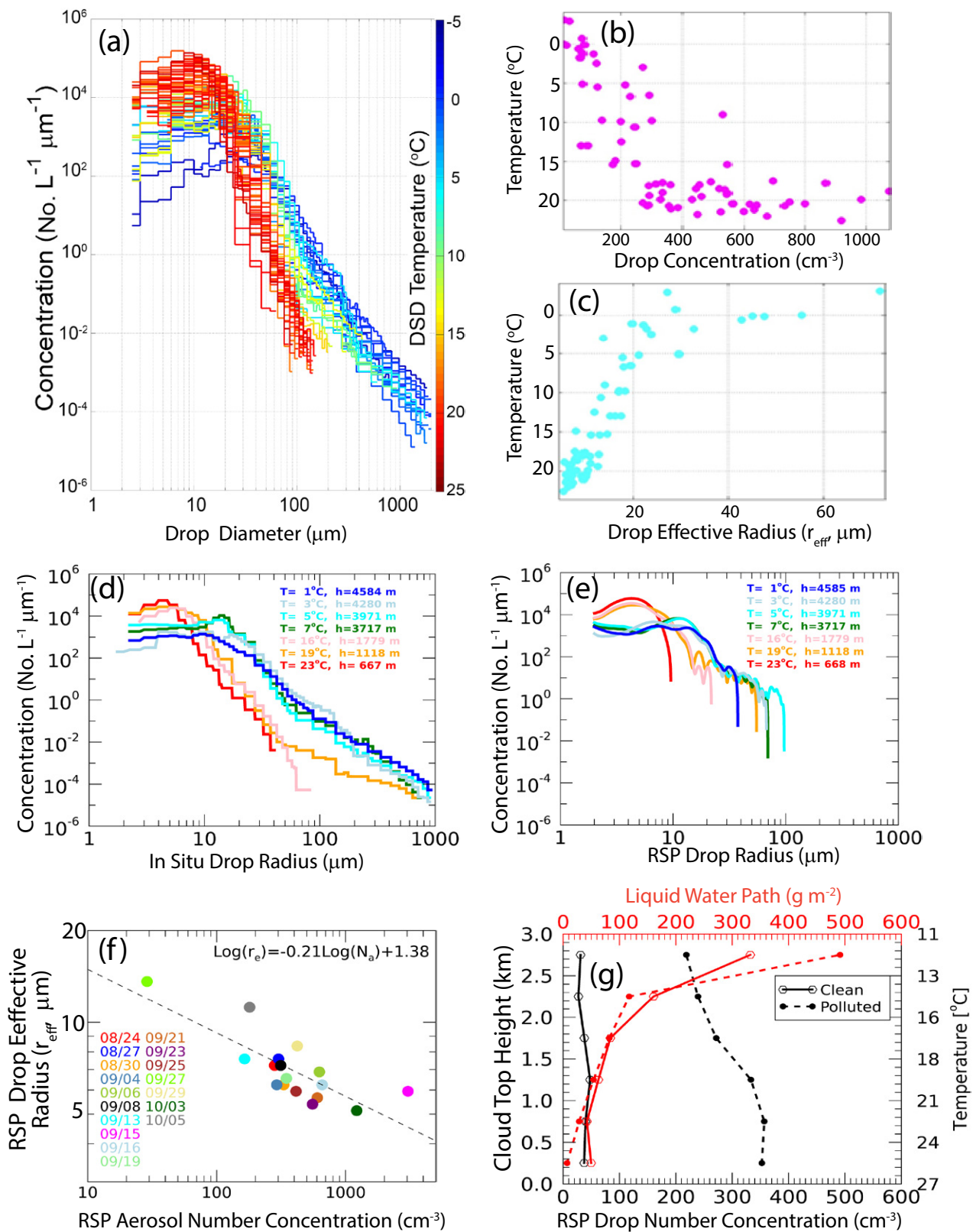


Fig. 6. In situ and RSP-retrieved observations of cloud properties as a function of temperature, aerosol loading, and height. Included are P-3- and Learjet 35-measured droplet (a) distributions, (b) number concentrations, and (c) effective radii ( $r_{\text{eff}}$ ) as a function of temperature. For reference, the 0°C melting level is  $\sim 4.7$  km in this region. The figure also shows cloud droplet size distributions comparisons by temperature of (d) Learjet 35 and (e) RSP, averaged for RSP footprints with cloud-top heights within 250 m of the in situ penetrations. As RSP is not sensitive to drops with radii greater than 100 μm, retrievals are truncated there. (f) Flight-average samples of RSP's retrievals of the low-cloud environments cloud droplet effective radius ( $r_{\text{eff}}$ ) vs its derived column aerosol number concentration. (g) Mean RSP-retrieved droplet number concentrations and liquid water paths as a function of cloud-top height for shallow cumulus in clean (solid, 5 Oct 2019, 1,521 clouds, RSP mean AOD = 0.08) and polluted (dashed, 19 Sep 2019, 5,545 clouds, mean AOD = 0.32) environments. Averages are taken over 500-m RSP cloud-top-height bins.



ability to identify coalescence by showing flight-average retrieved cloud-top  $r_{\text{eff}}$  matched to likewise retrieved aerosol number concentration, clearly demonstrating the Twomey effect. Current research is focusing on closing the strong dependencies of different stages of cloud development on cloud microphysical properties. For example, Fig. 6g shows RSP-retrieved droplet number concentrations and liquid water paths (LWPs) as a function of cloud-top height for shallow cumulus in clean and polluted environments. Droplet number concentrations are clearly larger in the polluted environment, while LWPs are similar. LWP approximately scales with the square of cloud-top height, as expected (Brenguier et al. 2000). Droplet number concentrations generally decrease with height, most likely because of collision–coalescence processes. These polarimetric data along with in situ, lidar, radar, and microwave data will provide new assessment capabilities of CNN’s role in cloud processes.

Cloud analyses such as those shown above must take in the context of their environment. Observed cloud fields were not random when viewed from larger vantage points. They had organized structure associated with monsoon conditions, thermodynamic state, and various forms of shear and low-level convergence. Figures 1c and 1h include fields of cumulus and congestus versus lines from convergence and confluence (Fig. 1d), land breezes (Fig. 1f), and cold pools (Fig. 1g). A particularly noteworthy feature was the prevalence of midlevel inversions and dry layers that often capped vigorous warm convection and created warm “altocumulus anvils.” Data collected on 7 September 2019, when a monsoon enhancement advected Borneo smoke into Luzon, were a good example. Figure 7a provides a *Terra* MODIS image (RGB mapped to 2.2, 0.87, and 0.44  $\mu\text{m}$ ), differentiating warm and deep clouds by coral and bright pink colors, respectively. Cloud morphology was largely in the form of thick altocumulus clouds generated by detrainment from underlying warm convection (Fig. 7b) beneath a strong 725-hPa inversion (Fig. 7c). Occasional turrets would build but then quickly decay, with deeper cells evolving with the help of onshore orographic effects on Luzon. A critical height may have been located at  $-14^{\circ}\text{C}$ , where significant ice production was detected in turret tops. The altocumulus layers (clearly observed by the W-band radar (Fig. 7d) obscured the intense isolated warm rain cells that fed them (Figs. 7e,f). The convection appeared so intense at times that the Ka-band reflectivity profile showed signs of full attenuation. Many cases of strong warm convection under inversions and altocumulus were sampled during CAMP<sup>2</sup>Ex, each with slightly different forcing agents, ranging from TC arms to weak convergence lines. Ongoing studies are investigating the nature of vertical transport and entrainment/detrainment processes within the context of this meteorology. To do so, samples such as shown here must be linked to where the cloud is in its life cycle (see section “The future of technology development and process level science”).

**Radiation.** Given the heterogeneous nature of the MC’s clouds (Hong and Di Girolamo 2020), with multiple cloud types and life cycles often present at the same location and time (e.g., Figs. 1 and 7), accurately assessing the radiation budget and interpreting satellite observations is extraordinarily difficult. It is necessary to account for the region’s ubiquitous cirrus, which affects all radiation-driven processes including air–sea interaction and MBL cloud systems, cloud-top cooling/instability, and diabatic heating rates. Cirrus cloud optical depth (COD) and AOD products were created using a new low-cost, spectral version of a sunshine pyranometer (SPN; Badosa et al. 2014; Wood et al. 2017; Norgren et al. 2022) mounted on the P-3. With no moving parts, the SPN makes measurements of downwelling total and diffuse spectral solar irradiance. Figure 8a shows that the derived COD at 860 nm were lognormal with a median value of 0.3. The derived broadband shortwave, longwave, and net cloud radiative effects at flight levels, defined as downwelling flux difference between cirrus and clear sky, are also shown, indicating that the pervasive cirrus has significant net radiative effects that should be accounted for in both basin-scale and high-resolution simulations, despite being very thin.

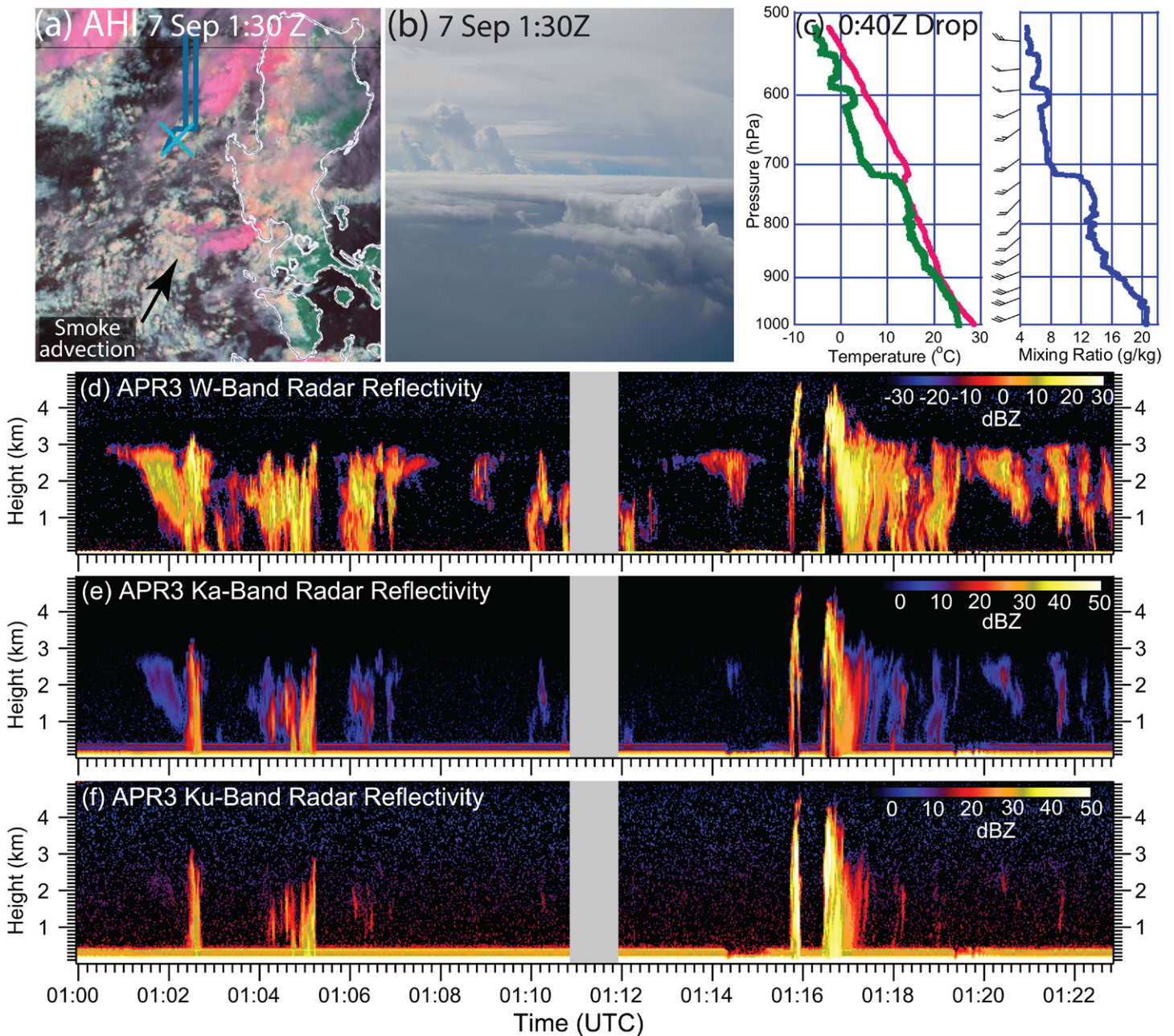


Fig. 7. An example of a monsoon enhancement period but with strong regional subsidence sampled on 7 Sep 2019. (a) AHI “ice enhancement” image at 0130 UTC (0930 local time), where bright pink indicates ice clouds, coral implies large water droplets, and white small water droplets (RGB mapped to 2.2, 0.87, and 0.44  $\mu\text{m}$ ). The light blue  $\times$  marks the P-3 location and ends the last 30 min of track (blue); (b) a cockpit photo of multiple cloud layers taken at the end of this segment, demonstrating the complex trilevel cloudiness of the region; (c) dropsonde temperature, dewpoint, and water vapor mixing ratio demonstrate the presence of a strong 725-hPa inversion with corresponding moist layer below it; (d)–(f) APR-3 W-, Ka-, and Ku-band cross sections from 0100 to 0123 UTC. The Ku-band radar is sensitive to large, precipitation-sized particles, while the Ka band is sensitive to smaller precipitation-sized particles and the W band is sensitive to cloud-sized particles.

A central CAMP<sup>2</sup>Ex objective was to evaluate benchmark data products relied on by the community. The areas of continued concern for constraining indirect effects and climate change–cloud feedbacks include multilayer cloud heterogeneity, the use of 1D versus 3D radiation (e.g., homogenous cloud assumptions), and unresolved (subpixel) cloud fields (e.g., IPCC 2013; Boeke et al. 2016). Limited imager resolution and cloud heterogeneity were expected to lead to erroneous satellite-derived cloud radiative effects. To evaluate current satellite capabilities in estimating surface radiation, CAMP<sup>2</sup>Ex investigators used the new “Education and Research 3D Radiative Transfer Toolbox” (EaR<sup>3</sup>T; Gristey et al. 2020; Chen et al. 2023)

to calculate shortwave irradiance from AHI geostationary satellite imagery cloud products along all P-3 flight tracks, and subsequently compared them to the irradiance measurements on board the P-3. Figure 8b shows this comparison for the downwelling irradiance at 745 nm for all flight legs below  $\sim 1,000$ -m altitude. It reveals satellite-based calculations underestimate the transmission by clouds by about 5%–10%, and that cloud-free regions (transmittance around 1) are rarely captured because, just like small clouds, small cloud gaps are also missed in coarse satellite pixels. Even larger discrepancies occur in the morning and evening hours when the sun elevation is low. The remaining discrepancies, including transmissions  $> 1$ , are primarily from 3D radiative effects. For the mitigation of 3D COD retrieval biases, a CNN retrieval shows promise (e.g., Nataraja et al. 2022), as does tomography (Levis et al. 2020).

CAMP<sup>2</sup>Ex’s airborne payloads and special orders for high-resolution imagery for marine environments offered further opportunities to evaluate and improve cloud products.

Figure 9a shows the 2 October 2019 *Terra*-MODIS overpass over small and densely populated low-level cumuli within a polluted Asian air mass (250-m resolution). The P-3 flight track and MODIS cloud  $r_{\text{eff}}$  retrievals are overlaid. For comparison, Terra-ASTER granule (60 km  $\times$  60 km, 15-m resolution) is within the red boxed subdomain (Fig. 9b). Subsequent overlays of MODIS 1-km imagery, cloud mask, cloud height, and cloud optical depth are provided in Figs. 9c–f. Clearly, most clouds are too small to be quantified by the 1-km MODIS standard algorithms, yet these small clouds dominate the top-of-atmosphere shortwave signal, raising questions of the fidelity of some cloud climatologies. While the MODIS retrievals work well for larger clouds, for fair weather scenes there is an accounting gap between large-scale reflectance and radiation products, and the individual clouds within the pixels. CAMP<sup>2</sup>Ex flight payloads were able to characterize scenes such as these with the combined RSP polarimeter and HSRL-2 lidar systems (Fig. 9g). Cloud stereography from RSP and the lidar system both provided similar values of  $\sim 500$  m in cloud height, both estimating cloud tops to be higher than the coarser and thermal IR based MODIS

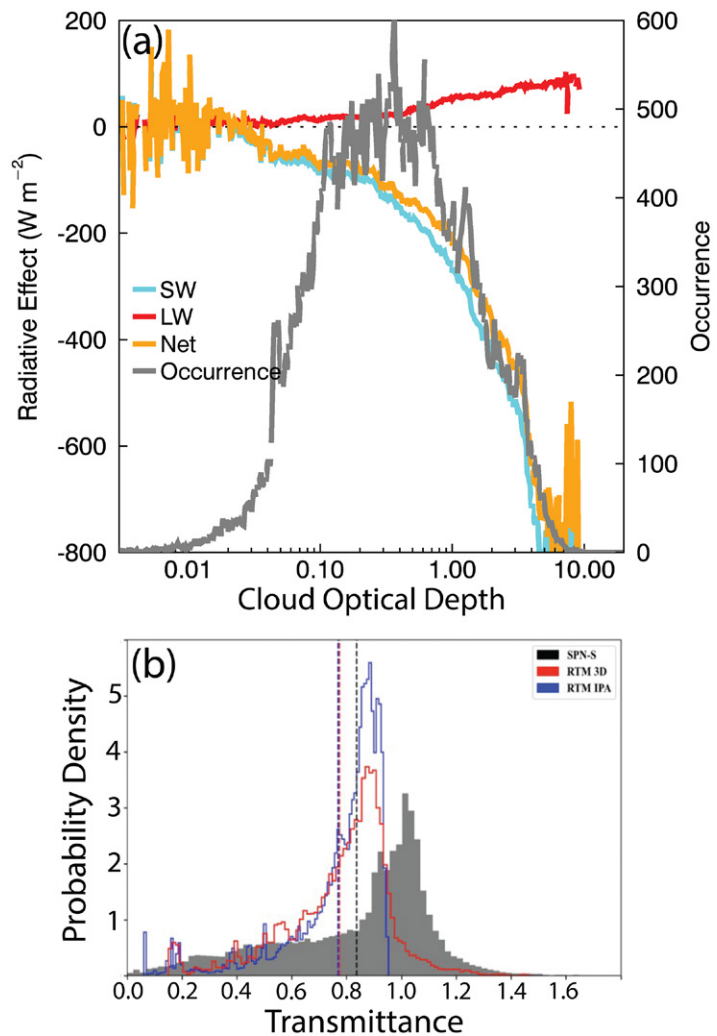


Fig. 8. SPN-inferred cloud and radiation properties over all flights. (a) Occurrence histograms of cirrus cloud optical depth and corresponding downward shortwave, longwave, and net effects at the time of cirrus observation for all flight legs above 5 km. (b) Probability density of corresponding shortwave transmittance inferred from the SPN instrument, as well as two geostationary satellite (AHI)-derived values from radiative transfer models including 3D radiative transfer and plane parallel. Transmittance values above 1.0 observed here are often indicative of 3D radiation effects, increasing toward sunrise and sunset.

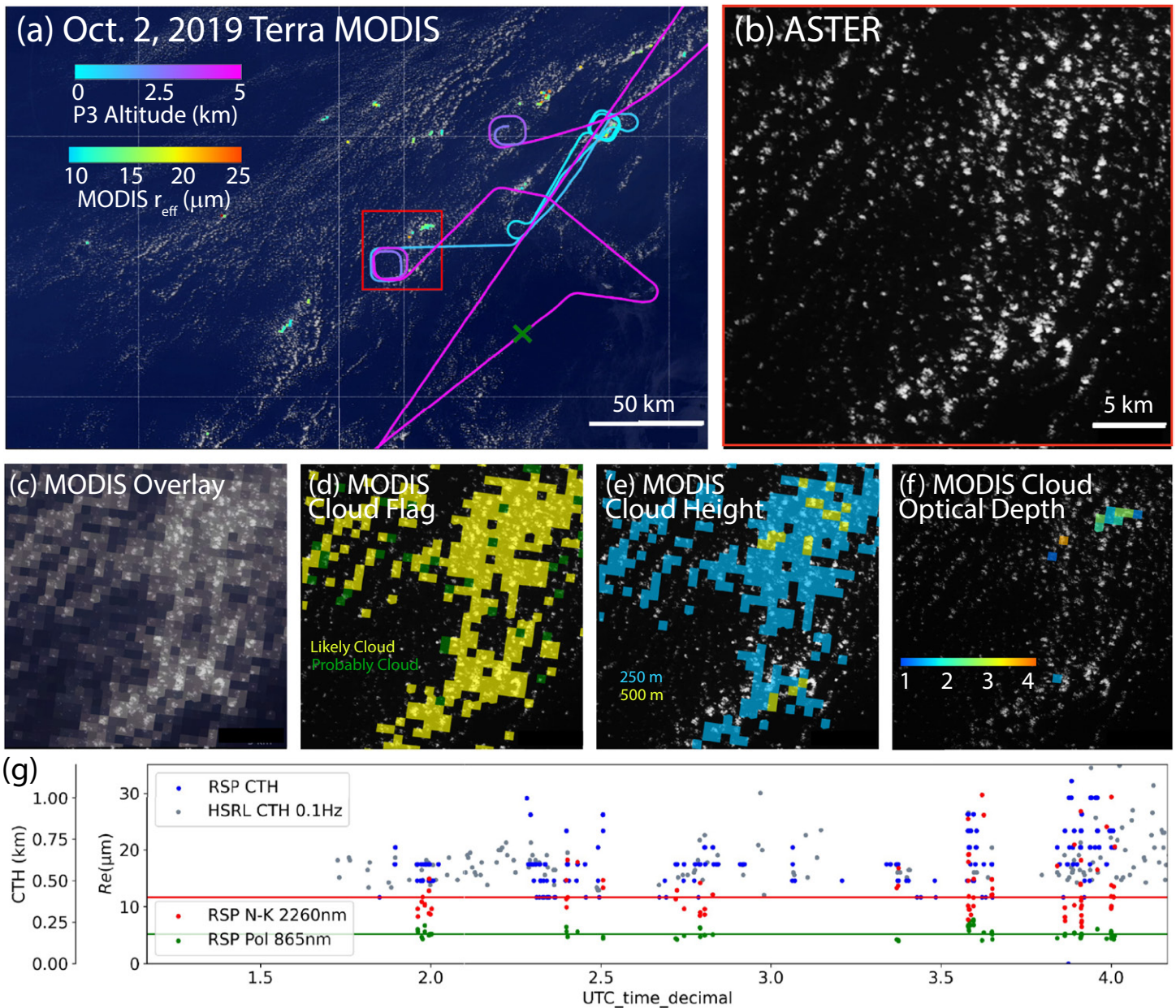


Fig. 9. Example comparison of MODIS 250-m imagery and 1-km cloud products to a collocated ASTER footprint to demonstrate sub-pixel-scale cloud effects for moderate resolution sensors. (a) P-3 flight track over a fair weather cumulus field. Also shown are the successful cloud effective radius retrievals. The green  $\times$  marks the P-3 location at overpass time. (b) Corresponding ASTER image (30m) marked as the red box in (a). (c)–(f) MODIS products projected onto the ASTER image including (c) 1-km grayscale, (d) the MODIS cloud flag, (e) cloud-height retrievals, and (f) cloud optical depth. (g) For comparison, HSRL-2 lidar and RSP parallax cloud-top heights as well as RSP cloud effective radius along the P-3 flight track are also shown.

retrievals. For cloud droplet  $r_{\text{eff}}$ , two retrieval types were performed by RSP and yielded values of  $\sim 5$  and  $\sim 11 \mu\text{m}$ . In comparison, the MODIS estimates of  $r_{\text{eff}}$  with what few observations are available yielded values of  $\sim 15 \mu\text{m}$ . Fu et al. (2022) provides an in-depth analysis of these differences for all coordinated MODIS and CAMP<sup>2</sup>Ex flights. These new polarimeter and high-resolution imagery technologies show promise to better constrain the cloud–radiation system.

### The future of technology development and process level science

The synopsis of CAMP<sup>2</sup>Ex presented here shows that science and technology are maturing to the point where we can now quantify the environment and important aerosol–cloud interaction outcomes within a complex monsoonal environment. Ongoing CAMP<sup>2</sup>Ex based

research is exploring ways to combine its extensive measurements, satellite retrievals, and model simulations to allow the community as a whole to make better use of the dataset. We use 24 September 2019 as a fitting concluding example of developing technologies to support future CAMP<sup>2</sup>Ex analyses. Figure 10a provides an image from the JPL data portal, including AHI imagery, a composite microwave rain indicator, and scatterometer winds along with the P-3, Learjet 35, and *Sally Ride* trajectories. Example regions of P-3-*Sally Ride* and P-3-Learjet collocation along this line are indicated by the orange and yellow boxes. Recall, the monsoon transition initiated around 21 September, and smoke influence over the NWTP had retreated southward, and the region was replaced by air masses more influenced by East Asian aerosol sources as well as some biomass burning smoke returning across the Philippines and back to the MC. PISTON SEA-POL radar data from the *Sally Ride* can be overlaid with a host of AHI derived products (cloud-top heights, temperatures, echo heights, etc., in Fig. 10b). Isolated

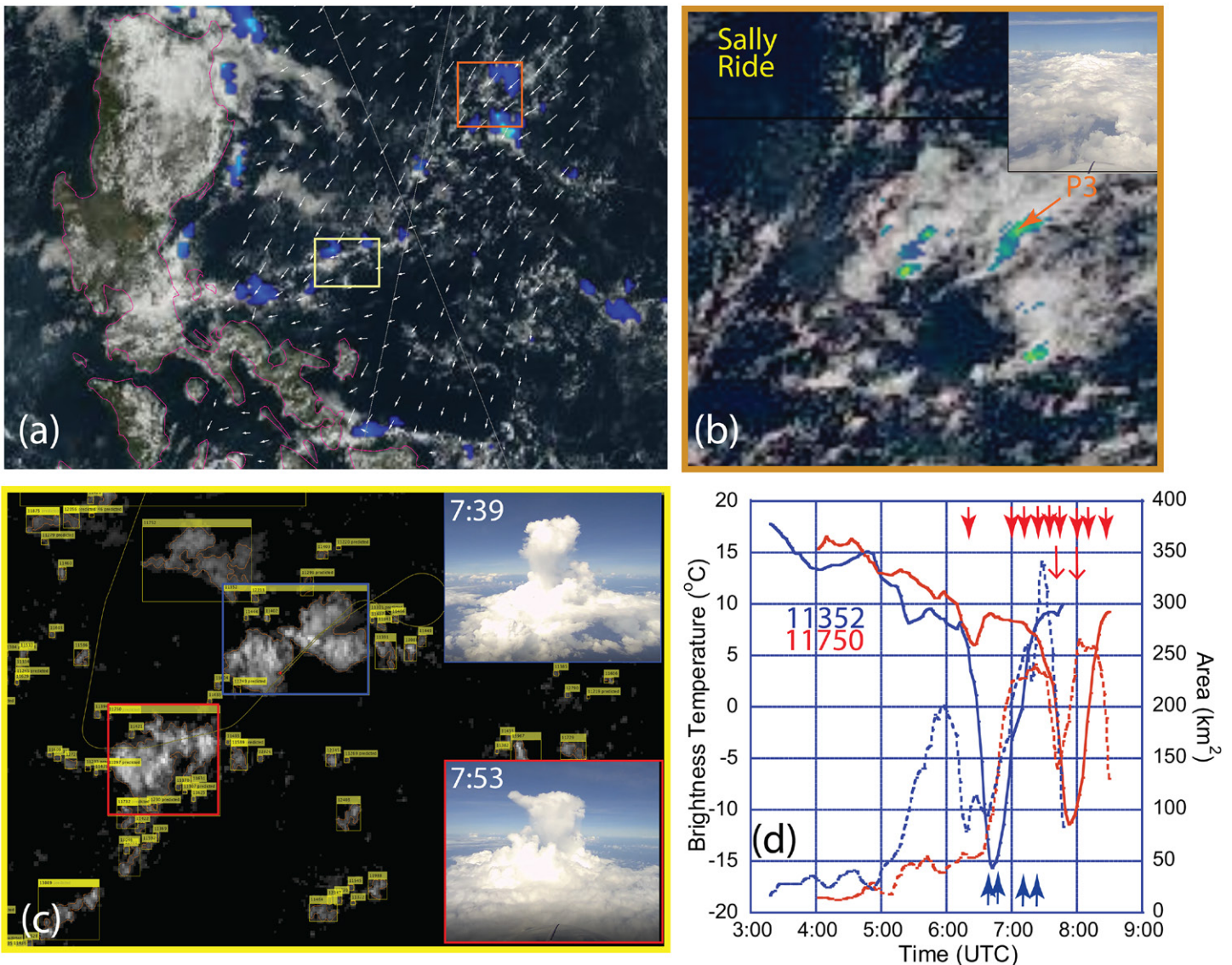


Fig. 10. (a) 24 Sep 2019 AHI RGB overview of the NWTP operations area, with microwave precipitation indicator and scatterometer winds. (b) Zoom of orange box on (a) indicating the P-3 location overlaid on SEA-POL radar reflectivity and AHI RGB. (c) Feature cloud objects tracked within the yellow domain in (a) for two congestus features, cloud 11352 (blue box) and cloud 11750 (red box), sampled by the aircraft. (d) Time series of corresponding cloud elements shown in (c) for cloud 11352 (blue) and cloud 11750 (red) for cloud spatial areas (dashed) and minimum brightness temperature as a proxy for cloud-top height (solid). Arrows indicate the times of cloud sampling by the P-3 (thick) and Learjet (thin). This demonstrates that for cloud sampling, the aircraft arrived at cloud 11352 just as it was maturing and measured its decay, but the aircraft was able to measure the full life cycle of cloud 11750. Without this technology, the team could not map the cloud observations to the modeled cloud life cycle.

cells of convection with tops to 3.5 km fed the development of altocumulus clouds, not unlike but more subdued than the case in Fig. 7. With these tools, analysts working with the P-3's nadir remote sensors know the spatial context of their observations.

Further CAMP<sup>2</sup>Ex development is gearing toward feature-based analysis to link observed outcomes to modeled processes. The persistent challenge of narrow-swath aircraft or polar/high-inclination satellite data are knowing where a cloud was in its life cycle at the time of sampling. This is particularly important to evaluate cloud radar observations of say vertical velocity, entrainment/detrainment, and overall moisture transport. An observation of a cloud could be in its growth, mature, or decaying stage, and from aircraft or polar/high-inclination-orbit satellites it is difficult to know what that measurement represents. Indeed, knowing where a cloud is in its life cycle is necessary to link the observations to modeling studies. This new cloud tracking technology demonstrates, for the 24 September case, when congestus turrets were penetrating the inversion as the P-3 rendezvoused with the Learjet 35. Using optical flow technology (see supplemental section S.3.3.3), individual cloud elements are identified and tracked (Fig. 10c). Two morphing cloud elements were observed by the aircraft (blue cloud: 11352; red cloud: 11750), with corresponding time series of cloud-top brightness temperature and points of sampling (Fig. 10d; thick arrow P-3, thin Learjet). Adding forward video shows how short-lived this population of congestus were, with turrets to 8 km developing over 30 min, and then evaporating over a similarly short time period. Also evident is the challenge and opportunity of the aircraft observations. For example, the P-3 flew to this environment because 11352 was observed to be growing, but arrived just as it matured. However, as this cloud was in decay, nearby cloud 11750 had its full life cycle observed by both aircraft. Such observations can then be compared to similar feature-oriented analyses of cloud simulations, such as the ongoing use and development of the Tracking and Object-Based Analysis of Clouds system for RAMS CAMP<sup>2</sup>Ex simulations (TOBAC; Heikenfeld et al. 2019), and interpreted in the context of their overall meteorological regime.

The technology demonstrated above, when combined with CAMP<sup>2</sup>Ex's and PISTON's other observation, satellite, and model informatics efforts, is taking Earth system science from simple observation to the coupled model processes that improve our understanding and prediction of the Earth system. In the future, research will migrate to more interdisciplinary topics enabled by new technology development, such as those associated with CAMP<sup>2</sup>Ex. A particularly important theme in the MC for future work will be the analysis of R/V *Sally Ride* and aircraft data to investigate diurnal forcing of coupled processes, which are driven by radiation relationships to clouds, air–sea interaction and possibly with composition feedbacks. Diurnal maritime convection was often visible in AHI imagery, as was diurnal maritime boundary layer variability during PISTON (e.g., de Szoeke et al. 2021). These are driven by diurnal warm layers at the sea surface, part of an energetic local air–sea feedback, and intensively measured during PISTON (Hughes et al. 2020a,b, 2021). Yet, while temporally categorized modes of convection are easy to identify in long-term satellite-based statistics (e.g., Yang and Smith 2008), limited radar/radiometer coverage, diurnally varying biases in geostationary data (Benas et al. 2019), and synoptic and mesoscale influences, including overlying cirrus, makes isolating diurnal processes a challenge (e.g., Snodgrass et al. 2009; Noel et al. 2018). CAMP<sup>2</sup>Ex and its partners now have the data, the tools, and the models to better understand and predict coupled maritime environments and to help design the satellite observing systems of the future.

**Acknowledgments.** This paper is dedicated to our dear friend and colleague Gemma Narisma, CAMP<sup>2</sup>Ex co-lead and director of the Manila Observatory, who passed away in 2021. CAMP<sup>2</sup>Ex could only be performed with her persistent effort and the cooperation of many Philippine entities

including PAGASA, the Department of Foreign Affairs (DFA), Philippine Department of Science and Technology (DOST), Civil Aviation Authorities of the Philippines (CAAP), and Armed Forces Philippines (AFP). We are also grateful to the U.S. Embassy in Manila Economics and Science Department for shepherding the mission over many years of preparation. The CAMP<sup>2</sup>Ex deployment was an enormous logistical undertaking, and all team members are most appreciative to the Earth Science Project Office. Likewise, the complex task of integrating, deploying, and flying the P-3 fell upon Wallops Flight Facility with additional operations and instrumentation support from NASA's Airborne Science Program and National Suborbital Research Center. CAMP<sup>2</sup>Ex's large and impactful NASA outreach effort was led by Bay Area Environmental, the Manila Observatory, and the U.S. Embassy. Major funding for CAMP<sup>2</sup>Ex was provided by the NASA Radiation Sciences Program, the U.S. Naval Research Laboratory Base Program, and numerous sponsors to the Manila Observatory. Cooperative funding with PISTON was provided by the Office of Naval Research. Finally, each CAMP<sup>2</sup>Ex PI was supported by their own team, including early career scientists and students. Additional acknowledgments are provided in supplemental section S.4.

**Data availability statement.** The CAMP<sup>2</sup>Ex data doi is <https://doi.org/10.5067/Suborbital/CAMP2EX2018/DATA001> with access available at <https://www-air.larc.nasa.gov/missions/camp2ex/index.html>. Additional descriptive and satellite data can be found on the JPL data portal (<https://camp2ex.jpl.nasa.gov/>) and the University of Wisconsin geoworldview site (<http://geoworldview.ssec.wisc.edu/>). The PISTON dataset can also be found at the LaRC site (<https://www-air.larc.nasa.gov/cgi-bin/ArcView/camp2ex?RV-SALLY-RIDE=1>), at <https://doi.org/10.5067/SUBORBITAL/PISTON2018-ONR-NOAA/RVTHOMPSON/DATA001> for 2018 and <https://doi.org/10.5067/SUBORBITAL/PISTON2019-ONR-NOAA/RVSALLYRIDE/DATA001> for 2019, as well as at the official mission site, <https://onrpiston.colostate.edu/>.

## References

- Ackerman, A. S., O. B. Toon, D. E. Stevens, A. J. Heymsfield, V. Ramanathan, and E. J. Welton, 2000: Reduction of tropical cloudiness by soot. *Science*, **288**, 1042–1047, <https://doi.org/10.1126/science.288.5468.1042>.
- Akagi, S. K., R. J. Yokelson, C. Wiedinmyer, M. J. Alvarado, J. S. Reid, T. Karl, J. D. Crounse, and P. O. Wennberg, 2011: Emission factors for open and domestic biomass burning for use in atmospheric models. *Atmos. Chem. Phys.*, **11**, 4039–4072, <https://doi.org/10.5194/acp-11-4039-2011>.
- Alexandrov, M. D., B. Cairns, C. Emde, A. S. Ackerman, and B. van Diedenhoven, 2012a: Accuracy assessments of cloud droplet size retrievals from polarized reflectance measurements by the research scanning polarimeter. *Remote Sens. Environ.*, **125**, 92–111, <https://doi.org/10.1016/j.rse.2012.07.012>.
- , —, and M. I. Mishchenko, 2012b: Rainbow Fourier transform. *J. Quant. Spectrosc. Radiat. Transfer*, **113**, 2521–2535, <https://doi.org/10.1016/j.jqsrt.2012.03.025>.
- Altaratz, O., I. Koren, T. Reisin, A. Kostinski, G. Feingold, Z. Levin, and Y. Yin, 2008: Aerosols' influence on the interplay between condensation, evaporation and rain in warm cumulus cloud. *Atmos. Chem. Phys.*, **8**, 15–24, <https://doi.org/10.5194/acp-8-15-2008>.
- Andreae, M. O., D. Rosenfeld, P. Artaxio, A. A. Costa, G. P. Frank, K. M. Longo, and M. A. F. Silva-Dias, 2004: Smoking rain clouds over the Amazon. *Science*, **303**, 1337–1342, <https://doi.org/10.1126/science.1092779>.
- Atwood, S. A., and Coauthors, 2017: Size-resolved aerosol and cloud condensation nuclei (CCN) properties in the remote marine South China Sea – Part 1: Observations and source classification. *Atmos. Chem. Phys.*, **17**, 1105–1123, <https://doi.org/10.5194/acp-17-1105-2017>.
- Badosa, J., J. Wood, P. Blanc, C. N. Long, L. Vuilleumier, D. Demengel, and M. Haefelin, 2014: Solar irradiances measured using SPN1 radiometers: Uncertainties and clues for development. *Atmos. Meas. Tech.*, **7**, 4267–4283, <https://doi.org/10.5194/amt-7-4267-2014>.
- Bagtasa, G., 2020: 118-year climate and extreme weather events of Metropolitan Manila in the Philippines. *Int. J. Climatol.*, **40**, 1228–1240, <https://doi.org/10.1002/joc.6267>.
- Balasubramanian, R., W.-B. Qian, S. Decesari, M. C. Facchini, and S. Fuzzi, 2003: Comprehensive characterization of PM<sub>2.5</sub> aerosols in Singapore. *J. Geophys. Res.*, **108**, 4523, <https://doi.org/10.1029/2002JD002517>.
- Benas, N., J. F. Meirink, M. Stengel, and P. Stammes, 2019: Sensitivity of liquid cloud optical thickness and effective radius retrievals to cloud bow and glory conditions using two SEVIRI imagers. *Atmos. Meas. Tech.*, **12**, 2863–2879, <https://doi.org/10.5194/amt-12-2863-2019>.
- Berg, W., T. L'Ecuyer, and S. van den Heever, 2008: Evidence for the impact of aerosols on the onset and microphysical properties of rainfall from a combination of satellite observations and cloud-resolving model simulations. *J. Geophys. Res.*, **113**, D14S23, <https://doi.org/10.1029/2007JD009649>.
- Bessho, K., and Coauthors, 2016: An introduction to Himawari-8/9 – Japan's new-generation geostationary meteorological satellites. *J. Meteor. Soc. Japan*, **94**, 151–183, <https://doi.org/10.2151/jmsj.2016-009>.
- Boeke, R. C., A. M. Allan, and J. A. Coakley Jr., 2016: Properties of marine stratocumulus obtained with partly cloudy pixel retrievals and found in the MODIS MOD06 cloud product. *J. Geophys. Res. Atmos.*, **121**, 6404–6424, <https://doi.org/10.1002/2015JD024149>.
- Braun, R. A., and Coauthors, 2020: Long-range aerosol transport and impacts on size-resolved aerosol composition in Metro Manila, Philippines. *Atmos. Chem. Phys.*, **20**, 2387–2405, <https://doi.org/10.5194/acp-20-2387-2020>.
- Brenguier, J., H. Pawlowska, L. Schüller, R. Preusker, J. Fischer, and Y. Fouquart, 2000: Radiative properties of boundary layer clouds: Droplet effective radius versus number concentration. *J. Atmos. Sci.*, **57**, 803–821, [https://doi.org/10.1175/1520-0469\(2000\)057<0803:RPOBLC>2.0.CO;2](https://doi.org/10.1175/1520-0469(2000)057<0803:RPOBLC>2.0.CO;2).
- Burton, S. P., and Coauthors, 2016: Information content and sensitivity of the  $3\beta + 2\alpha$  lidar measurement system for aerosol microphysical retrievals. *Atmos. Meas. Tech.*, **9**, 5555–5574, <https://doi.org/10.5194/amt-9-5555-2016>.
- Carminati, F., P. Ricaud, J.-P. Pommereau, E. Rivière, S. Khaykin, J.-L. Attié, and J. Warner, 2014: Impact of tropical land convection on the water vapor budget in the tropical tropopause layer. *Atmos. Chem. Phys.*, **14**, 6195–6211, <https://doi.org/10.5194/acp-14-6195-2014>.
- Chang, C.-P., Z. Wang, J. McBride, and C. Liu, 2005: Annual cycle of Southeast Asia—Maritime Continent rainfall and the asymmetric monsoon transition. *J. Climate*, **18**, 287–301, <https://doi.org/10.1175/JCLI-3257.1>.
- Chen, H., K. S. Schmidt, S. T. Massie, V. H. Nataraja, M. Norgren, R. Holz, H. Iwabuchi, and J. Gristey, 2023: The Education and Research 3D Radiative Transfer Toolbox (EaR<sup>3</sup>T) – Towards the mitigation of 3D biases in airborne and spaceborne passive imagery cloud retrievals. *Atmos. Meas. Tech.*, **16**, 1971–2000, <https://doi.org/10.5194/amt-16-1971-2023>.
- Chen, Q., S. McGowen, C. Gouramanis, L. Fong, R. Balasubramanian, and D. Taylor, 2020: Rapidly rising transboundary atmospheric pollution from industrial and urban sources in Southeast Asia and its implications for regional sustainable development. *Environ. Res. Lett.*, **15**, 1040a5, <https://doi.org/10.1088/1748-9326/abb5ce>.
- Cinco, T. A., R. G. de Guzman, F. D. Hilario, and D. M. Wilson, 2014: Long-term trends and extremes in observed daily precipitation and near surface air temperature in the Philippines for the period 1951–2010. *Atmos. Res.*, **145–146**, 12–26, <https://doi.org/10.1016/j.atmosres.2014.03.025>.
- Clarke, A. D., Z. Ki, and M. Litchy, 1996: Aerosol dynamics in the equatorial Pacific marine boundary layer: Microphysics, diurnal cycles and entrainment. *Geophys. Res. Lett.*, **23**, 733–736, <https://doi.org/10.1029/96GL00778>.
- Clayson, C. A., and A. S. Bogdanoff, 2013: The effect of diurnal sea surface temperature warming on climatological air–sea fluxes. *J. Climate*, **26**, 2546–2556, <https://doi.org/10.1175/JCLI-D-12-00062.1>.
- Cotton, W. R., and Coauthors, 2003: RAMS 2001: Current status and future directions. *Meteor. Atmos. Phys.*, **82**, 5–29, <https://doi.org/10.1007/s00703-001-0584-9>.
- , G. M. Krall, and G. G. Carrio, 2012: Potential indirect effects of aerosol on tropical cyclone intensity: Convective fluxes and cold-pool activity. *Trop. Cyclone Res. Rev.*, **1**, 293–306, <https://doi.org/10.6057/2012TCRR03.05>.
- Crippa, P., and Coauthors, 2016: Population exposure to hazardous air quality due to the 2015 fires in Equatorial Asia. *Sci. Rep.*, **6**, 37074, <https://doi.org/10.1038/srep37074>.
- Cruz, F. T., G. T. Narisma, M. Q. Villafuerte, K. U. Cheng Chua, and L. M. Olaguera, 2013: A climatological analysis of the southwest monsoon rainfall in the Philippines. *Atmos. Res.*, **122**, 609–616, <https://doi.org/10.1016/j.atmosres.2012.06.010>.
- Cruz, M. T., and Coauthors, 2019: Size-resolved composition and morphology of particulate matter during the southwest monsoon in Metro Manila, Philippines. *Atmos. Chem. Phys.*, **19**, 10675–10696, <https://doi.org/10.5194/acp-19-10675-2019>.
- Deni, S. M., J. Suhaila, W. Z. Wan Zin, and A. A. Jemain, 2010: Spatial trends of dry spells over Peninsular Malaysia during monsoon seasons. *Theor. Appl. Climatol.*, **99**, 357–371, <https://doi.org/10.1007/s00704-009-0147-4>.
- de Szoeko, S. P., T. Marke, and W. A. Brewer, 2021: Diurnal ocean surface warming drives convective turbulence and clouds in the atmosphere. *Geophys. Res. Lett.*, **48**, e2020GL091299, <https://doi.org/10.1029/2020GL091299>.
- Dey, S., L. Di Girolamo, G. Zhao, A. L. Jones, and G. M. McFarquhar, 2011: Satellite-observed relationships between aerosol and trade-wind cumulus cloud properties over the Indian Ocean. *Geophys. Res. Lett.*, **38**, L01804, <https://doi.org/10.1029/2010GL045588>.
- Di Girolamo, L., and Coauthors, 2021: Data fusion visualization for NASA CAMP2Ex field campaign. Tech. Rep., 12 pp., <http://hdl.handle.net/2142/110095>.
- Endo, N., J. Matsumoto, and T. Lwin, 2009: Trends in precipitation extremes over Southeast Asia. *SOLA*, **5**, 168–171, <https://doi.org/10.2151/sola.2009-043>.
- Fairall, C. W., E. F. Bradley, J. S. Godfrey, G. A. Wick, J. B. Edson, and G. S. Young, 1996a: Cool-skin and warm-layer effects on sea surface temperature. *J. Geophys. Res.*, **101**, 1295–1308, <https://doi.org/10.1029/95JC03190>.



- , —, D. P. Rogers, J. B. Edson, and G. S. Young, 1996b: Bulk parameterization of air-sea fluxes for Tropical Ocean-Global Atmosphere Coupled-Ocean Atmosphere Response Experiment. *J. Geophys. Res.*, **101**, 3747–3764, <https://doi.org/10.1029/95JC03205>.
- Fan, J., L. R. Leung, D. Rosenfeld, Q. Chen, Z. Li, J. Zhang, and H. Yan, 2013: Microphysical effects determine the macrophysical response for aerosol impacts, on deep convective clouds. *Proc. Natl. Acad. Sci. USA*, **110**, E4581–E4590, <https://doi.org/10.1073/pnas.1316830110>.
- Field, R. D., and S. S. P. Shen, 2008: Predictability of carbon emissions from biomass burning in Indonesia from 1997 to 2006. *J. Geophys. Res.*, **113**, G04024, <https://doi.org/10.1029/2008JG000694>.
- , and Coauthors, 2016: Indonesian fire activity and smoke pollution in 2015 show persistent nonlinear sensitivity to El Niño induced drought. *Proc. Natl. Acad. Sci. USA*, **113**, 9204–9209, <https://doi.org/10.1073/pnas.1524888113>.
- Freud, E., and D. Rosenfeld, 2012: Linear relation between convective cloud drop number concentration and depth for rain initiation. *J. Geophys. Res.*, **117**, D02207, <https://doi.org/10.1029/2011JD016457>.
- Fu, D., and Coauthors, 2022: An evaluation of the liquid cloud droplet effective radius derived from MODIS, airborne remote sensing, and in situ measurements from CAMP<sup>2</sup>Ex. *Atmos. Chem. Phys.*, **22**, 8259–8285, <https://doi.org/10.5194/acp-22-8259-2022>.
- Grant, L. D., and S. C. van den Heever, 2015: Cold pool and precipitation responses to aerosol loading: Modulation by dry layers. *J. Atmos. Sci.*, **72**, 1398–1408, <https://doi.org/10.1175/JAS-D-14-0260.1>.
- Gristey, J. J., G. Feingold, I. B. Glenn, K. S. Schmidt, and H. Chen, 2020: On the relationship between shallow cumulus cloud field properties and surface solar irradiance. *Geophys. Res. Lett.*, **47**, e2020GL090152, <https://doi.org/10.1029/2020GL090152>.
- Gryspeerdt, E., and Coauthors, 2017: Constraining the instantaneous aerosol influence on cloud albedo. *Proc. Natl. Acad. Sci. USA*, **114**, 4899–4904, <https://doi.org/10.1073/pnas.1617765114>.
- Heikenfeld, M., P. J. Marinescu, M. Christensen, D. Watson-Parris, F. Senf, S. C. van den Heever, and P. Stier, 2019: tobac 1.2: Towards a flexible framework for tracking and analysis of clouds in diverse datasets. *Geosci. Model Dev.*, **12**, 4551–4570, <https://doi.org/10.5194/gmd-12-4551-2019>.
- Helfter, C., and A. H. Tremper, C. H. Halios, S. Kotthaus, A. Bjorkegren, C. S. B. Grimmond, J. F. Barlow, and E. Nemitz, 2016: Spatial and temporal variability of urban fluxes of methane, carbon monoxide and carbon dioxide above London, UK. *Atmos. Chem. Phys.*, **16**, 10543–10557, <https://doi.org/10.5194/acp-16-10543-2016>.
- Hersbach, H., and Coauthors, 2020: The ERA5 global reanalysis. *Quart. J. Roy. Meteor. Soc.*, **146**, 1999–2049, <https://doi.org/10.1002/qj.3803>.
- Hilario, M. R. A., and Coauthors, 2020: Characterizing weekly cycles of particulate matter in a coastal megacity: The importance of a seasonal, size-resolved, and chemically speciated analysis. *J. Geophys. Res. Atmos.*, **125**, e2020JD032614, <https://doi.org/10.1029/2020JD032614>.
- , and Coauthors, 2021: Measurement report: Long-range transport patterns into the tropical northwest Pacific during the CAMP<sup>2</sup>Ex aircraft campaign: Chemical composition, size distributions, and the impact of convection. *Atmos. Chem. Phys.*, **21**, 3777–3802, <https://doi.org/10.5194/acp-21-3777-2021>.
- Hong, Y., and L. Di Girolamo, 2020: Cloud phase characteristics over Southeast Asia from A-Train satellite observations. *Atmos. Phys. Chem.*, **20**, 8267–8291, <https://doi.org/10.5194/acp-20-8267-2020>.
- Hoppel, W. A., G. M. Frick, and R. E. Larson, 1986: Effect of nonprecipitating clouds in the aerosol size distribution in the marine boundary layer. *Geophys. Res. Lett.*, **13**, 125–128, <https://doi.org/10.1029/GL013i002p00125>.
- Hristova-Veleva, S., and Coauthors, 2020: An eye on the storm: Integrating a wealth of data for quickly advancing the physical understanding and forecasting of tropical cyclones. *Bull. Amer. Meteor. Soc.*, **101**, E1718–E1742, <https://doi.org/10.1175/BAMS-D-19-0020.1>.
- Huffman, G. J., and Coauthors, 2020: NASA Global Precipitation Measurement Integrated Multi-satellite Retrievals for GPM (IMERG). Algorithm Theoretical Basis Doc., version 6, 39 pp., [https://gpm.nasa.gov/sites/default/files/2020-05/IMERG\\_ATBD\\_V06.3.pdf](https://gpm.nasa.gov/sites/default/files/2020-05/IMERG_ATBD_V06.3.pdf).
- Hughes, K. G., J. N. Moum, and E. L. Shroyer, 2020a: Evolution of the velocity structure in the diurnal warm layer. *J. Phys. Oceanogr.*, **50**, 615–631, <https://doi.org/10.1175/JPO-D-19-0207.1>.
- , —, and —, 2020b: Heat transport through diurnal warm layers. *J. Phys. Oceanogr.*, **50**, 2885–2905, <https://doi.org/10.1175/JPO-D-20-0079.1>.
- , —, —, and W. D. Smyth, 2021: Stratified shear instabilities in diurnal warm layers. *J. Phys. Oceanogr.*, **51**, 2583–2598, <https://doi.org/10.1175/JPO-D-20-0300.1>.
- IPCC, 2013: *Climate Change 2013: The Physical Science Basis*. T. F. Stocker et al., Eds., Cambridge University Press, 1535 pp., <https://doi.org/10.1017/CBO9781107415324>.
- , 2014: *Climate Change 2014: Synthesis Report*. R. K. Pachauri and L. A. Meyer, Eds., IPCC, 151 pp.
- Jiang, X., T. Li, and B. Wang, 2004: Structures and mechanisms of the northward propagating boreal summer intraseasonal oscillation. *J. Climate*, **17**, 1022–1039, [https://doi.org/10.1175/1520-0442\(2004\)017<1022:SAMOTN>2.0.CO;2](https://doi.org/10.1175/1520-0442(2004)017<1022:SAMOTN>2.0.CO;2).
- Jin, F.-F., and B. J. Hoskins, 1995: The direct response to tropical heating in a baroclinic atmosphere. *J. Atmos. Sci.*, **52**, 307–319, [https://doi.org/10.1175/1520-0469\(1995\)052<0307:TDRTH>2.0.CO;2](https://doi.org/10.1175/1520-0469(1995)052<0307:TDRTH>2.0.CO;2).
- Johnson, R. H., T. M. Rickenbach, S. A. Rutledge, P. E. Ciesielski, and W. H. Schubert, 1999: Trimodal characteristics of tropical convection. *J. Climate*, **12**, 2397–2418, [https://doi.org/10.1175/1520-0442\(1999\)012<2397:TCOTC>2.0.CO;2](https://doi.org/10.1175/1520-0442(1999)012<2397:TCOTC>2.0.CO;2).
- Khain, A., D. Rosenfeld, and A. Pokrovsky, 2005: Aerosol impact on the dynamics and microphysics of deep convective clouds. *Quart. J. Roy. Meteor. Soc.*, **131**, 2639–2663, <https://doi.org/10.1256/qj.04.62>.
- , N. BenMoshe, and A. Pokrovsky, 2008: Factors determining the impacts of aerosols on surface precipitation from clouds: An attempt at classification. *J. Atmos. Sci.*, **65**, 1721–1748, <https://doi.org/10.1175/2007JAS2515.1>.
- Kim, P. S., D. J. Jacob, L. J. Mickley, S. N. Kopplitz, M. E. Marlier, R. S. DeFries, S. S. Myers, and Y. H. Mao, 2015: Sensitivity of population smoke exposure to fire locations in Equatorial Asia. *Atmos. Environ.*, **102**, 11–17, <https://doi.org/10.1016/j.atmosenv.2014.09.045>.
- Konwar, M., and R. S. Mahes Kumar, J. R. Kulkarni, E. Freud, B. N. Goswami, and D. Rosenfeld, 2012: Aerosol control on depth of warm rain in convective clouds. *J. Geophys. Res.*, **117**, D13204, <https://doi.org/10.1029/2012JD017585>.
- Kopplitz, S. N., and Coauthors, 2016: Public health impacts of the severe haze in Equatorial Asia in September–October 2015: Demonstration of a new framework for informing fire management strategies to reduce downwind smoke exposure. *Environ. Res. Lett.*, **11**, 094023, <https://doi.org/10.1088/1748-9326/11/9/094023>.
- , D. J. Jacob, M. P. Sulprizio, L. Myllyvirta, and C. Reid, 2017: Burden of disease from rising coal-fired power plant emissions in Southeast Asia. *Environ. Sci. Technol.*, **51**, 1467–1476, <https://doi.org/10.1021/acs.est.6b03731>.
- Lee, H.-H., O. Iraqi, Y. Gu, S. H.-L. Yim, A. Chulakadabba, A. Y.-M. Tonks, Z. Yang, and C. Wang, 2018: Impacts of air pollutants from fire and non-fire emissions on the regional air quality in Southeast Asia. *Atmos. Chem. Phys.*, **18**, 6141–6156, <https://doi.org/10.5194/acp-18-6141-2018>.
- , —, and C. Wang, 2019: The impact of future fuel consumption on regional air quality in Southeast Asia. *Sci. Rep.*, **9**, 2648, <https://doi.org/10.1038/s41598-019-39131-3>.
- Lee, S. S., L. J. Donner, V. T. J. Phillips, and Y. Ming, 2008: The dependence of aerosol effects on clouds and precipitation on cloud-system organization, shear and stability. *J. Geophys. Res.*, **113**, D16202, <https://doi.org/10.1029/2007JD009224>.
- Leung, G., and S. C. van den Heever, 2022: Controls on the Development and Circulation of Terminal versus Transient Congestus Clouds and Implications for Midlevel Aerosol Transport. *J. Atmos. Sci.*, **79**, 3083–3101, <https://doi.org/10.1175/JAS-D-21-0314.1>.
- Levis, A., Y. Y. Schechner, A. B. Davis, and J. Loveridge, 2020: Multi-view polarimetric scattering cloud tomography and retrieval of droplet size. *Remote Sens.*, **12**, 2831, <https://doi.org/10.3390/rs12172831>.

- Li, W., C. Luo, D. Wang, and T. Lei, 2010: Diurnal variations of precipitation over the South China Sea. *Meteor. Atmos. Phys.*, **109**, 33–46, <https://doi.org/10.1007/s00703-010-0094-8>.
- Li, X., W.-K. Tao, H. Masunaga, G. Gu, and X. Zeng, 2013: Aerosol effects on cumulus congestus population over the tropical Pacific: A cloud-resolving modeling study. *J. Meteor. Soc. Japan*, **91**, 817–833, <https://doi.org/10.2151/jmsj.2013-607>.
- Lynch, P., and Coauthors, 2016: An 11-year global gridded aerosol optical thickness reanalysis (v1.0) for atmospheric and climate sciences. *Geosci. Model Dev.*, **9**, 1489–1522, <https://doi.org/10.5194/gmd-9-1489-2016>.
- Lyons, W. A., T. E. Nelson, E. R. Williams, J. A. Cramer, and T. R. Turner, 1998: Enhanced positive cloud-to-ground lightning in thunderstorms ingesting smoke from fires. *Science*, **282**, 77–80, <https://doi.org/10.1126/science.282.5386.77>.
- Mace, G. G., and A. C. Abernathy, 2016: Observational evidence for aerosol invigoration in shallow cumulus downstream of Mount Kilauea. *Geophys. Res. Lett.*, **43**, 2981–2988, <https://doi.org/10.1002/2016GL067830>.
- Matsui, T., H. Masunaga, S. M. Kreidenweis, R. A. Pielke Sr., W.-K. Tao, M. Chin, and Y. J. Kaufman, 2006: Satellite-based assessment of marine low cloud variability associated with aerosol, atmospheric stability, and the diurnal cycle. *J. Geophys. Res.*, **111**, D17204, <https://doi.org/10.1029/2005JD006097>.
- May, P. T., V. N. Bringi, and M. Thurai, 2011: Do we observe aerosol impacts on DSDs in strongly forced tropical thunderstorms? *J. Atmos. Sci.*, **68**, 1902–1910, <https://doi.org/10.1175/2011JAS3617.1>.
- Miettinen, J., C. Shi, and S. C. Liew, 2016: Land cover distribution in the peatlands of Peninsular Malaysia, Sumatra and Borneo in 2015 with changes since 1990. *Global Ecol. Conserv.*, **6**, 67–78, <https://doi.org/10.1016/j.gecco.2016.02.004>.
- Minobe, S., J. H. Park, and K. S. Virts, 2020: Diurnal cycles of precipitation and lighting in the tropics observed by TRMM3G68, GSMaP, LIS, and WWLLN. *J. Climate*, **33**, 4293–4313, <https://doi.org/10.1175/JCLI-D-19-0389.1>.
- Moran, K., S. Pezoa, C. W. Fairall, C. Williams, T. Ayers, A. Brewer, S. P. de Zoete, and V. Ghate, 2012: A motion-stabilized W-band radar for shipboard observations of marine boundary-layer clouds. *Bound.-Layer Meteor.*, **143**, 3–24, <https://doi.org/10.1007/s10546-011-9674-5>.
- Nara, H., H. Tanimoto, Y. Tohjima, H. Mukai, Y. Nojiri, and T. Machida, 2017: Emission factors of CO<sub>2</sub>, CO and CH<sub>4</sub> from Sumatran peatland fires in 2013 based on shipboard measurements. *Tellus*, **69B**, 1399047, <https://doi.org/10.1080/16000889.2017.1399047>.
- Nataraja, V., S. Schmidt, H. Chen, T. Yamaguchi, J. Kazil, G. Feingold, K. Wolf, and H. Iwabuchi, 2022: Segmentation-based multi-pixel cloud optical thickness retrieval using a convolutional neural network. *Atmos. Meas. Tech.*, **15**, 5181–5205, <https://doi.org/10.5194/amt-15-5181-2022>.
- National Academies of Sciences, Engineering, and Medicine, 2018: *Thriving on Our Changing Planet: A Decadal Strategy for Earth Observation from Space*. The National Academies Press, 716 pp., <https://doi.org/10.17226/24938>.
- Neale, R., and J. Slingo, 2003: The Maritime Continent and its role in the global climate: A GCM study. *J. Climate*, **16**, 834–848, [https://doi.org/10.1175/1520-0442\(2003\)016<0834:TMCAIR>2.0.CO;2](https://doi.org/10.1175/1520-0442(2003)016<0834:TMCAIR>2.0.CO;2).
- Nichol, J., 1998: Smoke haze in Southeast Asia: A predictable recurrence. *Atmos. Environ.*, **32**, 2715–2716, [https://doi.org/10.1016/S1352-2310\(98\)00086-7](https://doi.org/10.1016/S1352-2310(98)00086-7).
- Noel, V., H. Chepfer, M. Chiriaco, and J. Yorks, 2018: The diurnal cycle of cloud profiles over land and ocean between 51°S and 51°N, seen by the CATS spaceborne lidar from the International Space Station. *Atmos. Chem. Phys.*, **18**, 9457–9473, <https://doi.org/10.5194/acp-18-9457-2018>.
- Norgren, M. S., and Coauthors, 2022: Above-aircraft cirrus cloud and aerosol optical depth from hyperspectral irradiances measured by a total-diffuse radiometer. *Atmos. Meas. Tech.*, **15**, 1373–1394, <https://doi.org/10.5194/amt-15-1373-2022>.
- Olaguera, L. M., J. Matsumoto, H. Kubota, T. Inoue, E. O. Cayan, and F. D. Hilario, 2018: Interdecadal shifts in the winter monsoon rainfall of the Philippines. *Atmosphere*, **9**, 464, <https://doi.org/10.3390/atmos9120464>.
- Qian, J.-H., 2008: Why precipitation is mostly concentrated over islands in the Maritime Continent. *J. Atmos. Sci.*, **65**, 1428–1441, <https://doi.org/10.1175/2007JAS2422.1>.
- , A. W. Robertson, and V. Moron, 2010: Interactions among ENSO, the monsoon, and diurnal cycle in rainfall variability over Java, Indonesia. *J. Atmos. Sci.*, **67**, 3509–3524, <https://doi.org/10.1175/2010JAS3348.1>.
- Quinn, P. K., D. J. Coffman, J. E. Johnson, L. M. Upchurch, and T. S. Bates, 2017: Small fraction of marine cloud condensation nuclei made up of sea spray aerosol. *Nat. Geosci.*, **10**, 674–679, <https://doi.org/10.1038/ngeo3003>.
- Ramage, C. S., 1968: Role of a tropical “Maritime Continent” in the atmospheric circulation. *Mon. Wea. Rev.*, **96**, 365–370, [https://doi.org/10.1175/1520-0493\(1968\)096<0365:ROATMC>2.0.CO;2](https://doi.org/10.1175/1520-0493(1968)096<0365:ROATMC>2.0.CO;2).
- Reid, J. S., R. Koppmann, T. Eck, and D. Eleuterio, 2005: A review of biomass burning emissions part II: Intensive physical properties of biomass burning particles. *Atmos. Chem. Phys.*, **5**, 799–825, <https://doi.org/10.5194/acp-5-799-2005>.
- , and Coauthors, 2012: Multi-scale meteorological conceptual analysis of observed active fire hotspot activity and smoke optical depth in the Maritime Continent. *Atmos. Chem. Phys.*, **12**, 2117–2147, <https://doi.org/10.5194/acp-12-2117-2012>.
- , and Coauthors, 2013: Observing and understanding the Southeast Asian aerosol system by remote sensing: An initial review and analysis for the Seven Southeast Asian Studies (7SEAS) program. *Atmos. Res.*, **122**, 403–468, <https://doi.org/10.1016/j.atmosres.2012.06.005>.
- , and Coauthors, 2015: Observations of the temporal variability in aerosol properties and their relationships to meteorology in the summer monsoonal South China Sea/East Sea: The scale-dependent role of monsoonal flows, the Madden–Julian Oscillation, tropical cyclones, squall lines and cold pools. *Atmos. Chem. Phys.*, **15**, 1745–1768, <https://doi.org/10.5194/acp-15-1745-2015>.
- , and Coauthors, 2016a: Aerosol meteorology of the Maritime Continent for the 2012 7SEAS southwest monsoon intensive study – Part 1: Regional-scale phenomena. *Atmos. Chem. Phys.*, **16**, 14041–14056, <https://doi.org/10.5194/acp-16-14041-2016>.
- , and Coauthors, 2016b: Aerosol meteorology of Maritime Continent for the 2012 7SEAS southwest monsoon intensive study – Part 2: Philippine receptor observations of fine-scale aerosol behavior. *Atmos. Chem. Phys.*, **16**, 14057–14078, <https://doi.org/10.5194/acp-16-14057-2016>.
- , and Coauthors, 2019: Observations and hypotheses related to low to middle free tropospheric aerosol, water vapor and altocumulus cloud layers within convective weather regimes: A SEAC<sup>4</sup>RS case study. *Atmos. Chem. Phys.*, **19**, 11413–11442, <https://doi.org/10.5194/acp-19-11413-2019>.
- Rosenfeld, D., 1999: TRMM observed first direct evidence of smoke from forest fires inhibiting rainfall. *Geophys. Res. Lett.*, **26**, 3105–3108, <https://doi.org/10.1029/1999GL006066>.
- , and I. M. Lensky, 1998: Satellite-based insights into precipitation formation processes in continental and maritime convective clouds. *Bull. Amer. Meteor. Soc.*, **79**, 2457–2476, [https://doi.org/10.1175/1520-0477\(1998\)079<2457:SBIIPF>2.0.CO;2](https://doi.org/10.1175/1520-0477(1998)079<2457:SBIIPF>2.0.CO;2).
- Ross, A. D., R. E. Holz, G. Quinn, J. S. Reid, P. Xian, F. J. Turk, and D. J. Posselt, 2018: Exploring the first aerosol indirect effect over Southeast Asia using a 10-year collocated MODIS, CALIOP, and model dataset. *Atmos. Chem. Phys.*, **18**, 12747–12764, <https://doi.org/10.5194/acp-18-12747-2018>.
- Ruppert, J. H., 2016: Diurnal timescale feedbacks in the tropical cumulus regime. *J. Adv. Model. Earth Syst.*, **8**, 1483–1500, <https://doi.org/10.1002/2016MS000713>.
- Ruppert, J. H., Jr., and R. H. Johnson, 2015: Diurnally modulated cumulus moistening in the preonset stage of the Madden–Julian Oscillation during DYNAMO. *J. Atmos. Sci.*, **72**, 1622–1647, <https://doi.org/10.1175/JAS-D-14-0218.1>.
- Rutledge, S. A., V. Chandrasekar, B. Fuchs, J. George, F. Junyent, B. Dolan, P. C. Kennedy, and K. Drushka, 2019: SEA-POL goes to sea. *Bull. Amer. Meteor. Soc.*, **100**, 2285–2301, <https://doi.org/10.1175/BAMS-D-18-0233.1>.
- Saleeby, S. M., and S. C. van den Heever, 2013: Developments in the CSU-RAMS aerosol model: Emissions, nucleation, regeneration, deposition, and radiation. *J. Appl. Meteor. Climatol.*, **52**, 2601–2622, <https://doi.org/10.1175/JAMC-D-12-0312.1>.
- , W. Berg, S. C. van den Heever, and T. L’Ecuyer, 2010: Impact of cloud-nucleating aerosols in cloud-resolving model simulations of warm-rain precipitation in the East China Sea. *J. Atmos. Sci.*, **67**, 3916–3930, <https://doi.org/10.1175/2010JAS3528.1>.

- Sassen, K., and Z. Wang, 2012: The clouds of the middle troposphere: Composition, radiative impact, and global distribution. *Surv. Geophys.*, **33**, 677–691, <https://doi.org/10.1007/s10712-011-9163-x>.
- Sessions, W. R., and Coauthors, 2015: Development towards a global operational aerosol consensus: Basic climatological characteristics of the International Cooperative for Aerosol Prediction Multi-Model Ensemble (ICAP-MME). *Atmos. Chem. Phys.*, **15**, 335–362, <https://doi.org/10.5194/acp-15-335-2015>.
- Sheffield, A. M., S. M. Saleeby, and S. C. van den Heever, 2015: Aerosol-induced mechanisms for cumulus congestus growth. *J. Geophys. Res. Atmos.*, **120**, 8941–8952, <https://doi.org/10.1002/2015JD023743>.
- Shingler, T., and Coauthors, 2016: Ambient observations of hygroscopic growth factor and  $f(\text{RH})$  below 1: Case studies from surface and airborne measurements. *J. Geophys. Res. Atmos.*, **121**, 13 661–13 677, <https://doi.org/10.1002/2016JD025471>.
- Snodgrass, E. R., L. Di Girolamo, and R. M. Rauber, 2009: Precipitation characteristics of trade wind clouds during RICO derived from radar, satellite, and aircraft measurements. *J. Appl. Meteor. Climatol.*, **48**, 464–483, <https://doi.org/10.1175/2008JAMC1946.1>.
- Sobel, A. H., J. Sprintall, E. D. Maloney, Z. K. Martin, S. Wang, S. P. de Szoeke, B. C. Trabling, and S. A. Rutledge, 2021: Large-scale state and evolution of the atmosphere and ocean during PISTON 2018. *J. Climate*, **34**, 5017–5035, <https://doi.org/10.1175/JCLI-D-20-0517.1>.
- Sokolowsky, G. A., S. W. Freeman, and S. C. van den Heever, 2022: Sensitivities of maritime tropical trimodal convection to aerosols and boundary layer static stability. *J. Atmos. Sci.*, **79**, 2549–2570, <https://doi.org/10.1175/JAS-D-21-0260.1>.
- Sorooshian, A., G. Feingold, M. D. Lebsock, H. Jiang, and G. L. Stephens, 2009: On the precipitation susceptibility of clouds to aerosol perturbations. *Geophys. Res. Lett.*, **36**, L13803, <https://doi.org/10.1029/2009GL038993>.
- , Z. Wang, G. Feingold, and T. S. L'Ecuyer, 2013: A satellite perspective on cloud water to rain water conversion rates and relationships with environmental conditions. *J. Geophys. Res. Atmos.*, **118**, 6643–6650, <https://doi.org/10.1002/jgrd.50523>.
- Stahl, C., and Coauthors, 2020: An annual time series of weekly size-resolved aerosol properties in the megacity of Metro Manila, Philippines. *Sci. Data*, **7**, 128, <https://doi.org/10.1038/s41597-020-0466-y>.
- , and Coauthors, 2021: Total organic carbon and the contribution from speciated organics in cloud water: Airborne data analysis from the CAMP<sup>2</sup>Ex field campaign. *Atmos. Chem. Phys.*, **21**, 14 109–14 129, <https://doi.org/10.5194/acp-21-14109-2021>.
- Storer, R. L., S. C. van den Heever, and G. L. Stephens, 2010: Modeling aerosol impacts on convective storms in different environments. *J. Atmos. Sci.*, **67**, 3904–3915, <https://doi.org/10.1175/2010JAS3363.1>.
- , ———, and T. S. L'Ecuyer, 2014: Observations of aerosol-induced convective invigoration in the tropical east Atlantic. *J. Geophys. Res. Atmos.*, **119**, 3963–3975, <https://doi.org/10.1002/2013JD020272>.
- Tan, J., G. J. Huffman, D. T. Bolvin, and E. J. Nelkin, 2019: IMERG V06: Changes to the morphing algorithm. *J. Atmos. Oceanic Technol.*, **36**, 2471–2482, <https://doi.org/10.1175/JTECH-D-19-0114.1>.
- Tao, W.-K., X. Li, A. Khain, T. Matsui, S. Lang, and J. Simpson, 2007: Role of atmospheric aerosol concentration on deep convective precipitation: Cloud-resolving model simulations. *J. Geophys. Res.*, **112**, D24S18, <https://doi.org/10.1029/2007JD008728>.
- , J. P. Chen, Z. Li, C. Wang, and C. Zhang, 2012: Impact of aerosols on convective clouds and precipitation. *Rev. Geophys.*, **50**, RG2001, <https://doi.org/10.1029/2011RG000369>.
- Taufik, M., P. J. J. F. Torfs, R. Uijlenhoet, P. D. Jones, D. Murdiyarto, and H. A. J. Van Lanen, 2017: Amplification of wildfire area burnt by hydrological drought in the humid tropics. *Nat. Climate Change*, **7**, 428–431, <https://doi.org/10.1038/nclimate3280>.
- Thornton, J. A., K. S. Virts, R. H. Holzworth, and T. P. Mitchell, 2017: Lightning enhancement over major oceanic shipping lanes. *Geophys. Res. Lett.*, **44**, 9102–9111, <https://doi.org/10.1002/2017GL074982>.
- Twomey, S., 1974: Pollution and the planetary albedo. *Atmos. Environ.*, **8**, 1251–1256, [https://doi.org/10.1016/0004-6981\(74\)90004-3](https://doi.org/10.1016/0004-6981(74)90004-3).
- , 1977: The influence of pollution on the shortwave albedo of clouds. *J. Atmos. Sci.*, **34**, 1149–1152, [https://doi.org/10.1175/1520-0469\(1977\)034<1149:TIOPOT>2.0.CO;2](https://doi.org/10.1175/1520-0469(1977)034<1149:TIOPOT>2.0.CO;2).
- van den Heever, S. C., G. G. Carrió, W. R. Cotton, P. J. DeMott, and A. J. Prenni, 2006: Impacts of nucleating aerosol on Florida storms. Part I: Mesoscale simulations. *J. Atmos. Sci.*, **63**, 1752–1775, <https://doi.org/10.1175/JAS3713.1>.
- Villafuerte, M. Q., II, J. Matsumoto, and H. Kubota, 2014: Changes in extreme rainfall in the Philippines (1911–2010) linked to global mean temperature and ENSO. *Int. J. Climatol.*, **35**, 2033–2044, <https://doi.org/10.1002/joc.4105>.
- Wang, J., S. C. van den Heever, and J. S. Reid, 2009: A conceptual model for the link between Central American biomass burning aerosols and severe weather over south central United States. *Environ. Res. Lett.*, **4**, 015003, <https://doi.org/10.1088/1748-9326/4/1/015003>.
- , C. Gei, Z. Yang, E. J. Hyer, J. S. Reid, B. N. Chew, and M. Mahmud, 2013: Mesoscale modeling of smoke transport over the Southeast Asian Maritime Continent: Interplay of sea breeze, trade wind, typhoon, and topography. *Atmos. Res.*, **122**, 486–503, <https://doi.org/10.1016/j.atmosres.2012.05.009>.
- , M. Pikridas, T. Pinterich, S. R. Spielman, T. Tsang, A. McMahon, and S. Smith, 2017: A fast integrated mobility spectrometer for rapid measurement of sub-micrometer aerosol size distribution, Part II: Experimental characterization. *J. Aerosol Sci.*, **113**, 119–129, <https://doi.org/10.1016/j.jaerosci.2017.05.001>.
- Wang, Y., T. Pinterich, and J. Wang, 2018: Rapid measurement of sub-micrometer aerosol size distribution using a fast integrated mobility spectrometer. *J. Aerosol Sci.*, **121**, 12–20, <https://doi.org/10.1016/j.jaerosci.2018.03.006>.
- Wood, J., T. J. Smyth, and V. Estellés, 2017: Autonomous marine hyperspectral radiometers for determining solar irradiances and aerosol optical properties. *Atmos. Meas. Tech.*, **10**, 1723–1737, <https://doi.org/10.5194/amt-10-1723-2017>.
- Xian, P., J. S. Reid, S. A. Atwood, R. S. Johnson, E. J. Hyer, D. L. Westphal, and W. Sessions, 2013: Smoke aerosol transport patterns over the Maritime Continent. *Atmos. Res.*, **122**, 469–485, <https://doi.org/10.1016/j.atmosres.2012.05.006>.
- , and Coauthors, 2019: Current state of the global operational aerosol multi-model ensemble: An update from the International Cooperative for Aerosol Prediction (ICAP). *Quart. J. Roy. Meteor. Soc.*, **145**, 176–209, <https://doi.org/10.1002/qj.3497>.
- Xiao, Q., and Coauthors, 2023: New particle formation in the tropical free troposphere during CAMP2Ex: Statistics and impact of emission sources, convective activity, and synoptic condition. *Atmos. Chem. Phys. Discuss.*, <https://doi.org/10.5194/acp-2022-822>.
- Yang, S., and E. A. Smith, 2008: Convective-stratiform precipitation variability at seasonal scales from 8 yr of TRMM observations: Implications of multiple modes of diurnal variability. *J. Climate*, **21**, 4087–4114, <https://doi.org/10.1175/2008JCLI2096.1>.
- Yoneyama, K., and C. Zhang, 2020: Years of the Maritime Continent. *Geophys. Res. Lett.*, **47**, e2020GL087182, <https://doi.org/10.1029/2020GL087182>.
- Yuan, T., L. A. Remer, K. E. Pickering, and H. Yu, 2011: Observational evidence of aerosol enhancement of lightning activity and convective invigoration. *Geophys. Res. Lett.*, **38**, L04701, <https://doi.org/10.1029/2010GL046052>.
- Yusef, A. A., and H. Francisco, 2009: Climate change vulnerability mapping for Southeast Asia. EEPSEA Rep., 32 pp., <http://www.eepsea.org>.
- Zhang, C., 2005: The Madden-Julian Oscillation. *Rev. Geophys.*, **43**, RG2003, <https://doi.org/10.1029/2004RG000158>.